



Evaluation of video-based rPPG in challenging environments: Artifact mitigation and network resilience[☆]

Nhi Nguyen^{a,*}, Le Nguyen^a, Honghan Li^{a,b}, Miguel Bordallo López^{a,c},
Constantino Álvarez Casado^a

^a Center for Machine Vision and Signal Analysis (CMVS), University of Oulu, Oulu, Finland

^b Division of Bioengineering, Graduate School of Engineering Science, Osaka University, Osaka, Japan

^c VTT Technical Research Center of Finland Ltd., Oulu, Finland

ARTICLE INFO

Keywords:

Video-based remote photoplethysmography
Network resilience
Vital sign monitoring
Denoising techniques
Inpainting techniques
Artifact reduction

ABSTRACT

Video-based remote photoplethysmography (rPPG) has emerged as a promising technology for non-contact vital sign monitoring, especially under controlled conditions. However, the accurate measurement of vital signs in real-world scenarios faces several challenges, including artifacts induced by video codecs, low-light noise, degradation, low dynamic range, occlusions, and hardware and network constraints. In this article, a systematic and comprehensive investigation of these issues is conducted, measuring their detrimental effects on the quality of rPPG measurements. Additionally, practical strategies are proposed for mitigating these challenges to improve the dependability and resilience of video-based rPPG systems. Methods for effective biosignal recovery in the presence of network limitations are detailed, along with denoising and inpainting techniques aimed at preserving video frame integrity. Compared to previous studies, this paper addresses a broader range of variables and demonstrates improved accuracy across various rPPG methods, emphasizing generalizability for practical applications in diverse scenarios with varying data quality. Extensive evaluations and direct comparisons demonstrate the effectiveness of these approaches in enhancing rPPG measurements under challenging environments, contributing to the development of more reliable and effective remote vital sign monitoring technologies.

1. Introduction

Remote photoplethysmography (rPPG) marks a significant advancement in non-contact vital sign monitoring [1]. This approach, leveraging video-based techniques, enables the measurement of cardiovascular signals without requiring direct skin contact [2,3]. Particularly significant in the context of medical diagnostics, remote healthcare, or fitness, rPPG technology offers a non-intrusive and scalable solution for heart rate (HR) monitoring. Beyond physiological assessment, accurate and detailed rPPG signals can assess changes in the autonomic nervous system, capturing both arousal and valence components [4,5]. These measurements infer physical and mental activation levels, important for understanding emotional states and their impact on perception, learning, communication, and decision-making [5,6]. This capability can enhance applications in education, health monitoring, virtual reality, gaming, stress management, and safe machinery operation [4,7]. Enhanced multimodal emotion recognition systems using rPPG modality

can lead to more personalized and effective user experiences, especially in human–computer interactions (HCI). This integration is increasingly relevant with hybrid intelligent systems, which combine multiple data sources and processing techniques to create adaptive interfaces [6,8]. For instance, for users with visual or hearing impairments, understanding these emotional cues becomes even more critical. Emotional states significantly influence communication effectiveness and learning, areas where hearing-impaired individuals might experience particular challenges [9]. Integrating rPPG-based emotion recognition can help tailor the user experience in HCI systems by providing nuanced responses adapted to the emotional and physiological needs of hearing-impaired users [9,10]. This approach not only enhances accessibility but also ensures that the technology serves a broader range of user needs, making it a versatile tool in both specialized and everyday contexts [9]. However, the practical implementation of video-based

[☆] This research has been supported by the Academy of Finland 6G Flagship program under Grant 346208 and PROFi5 HiDyn under Grant 326291 and JSPS (Japan Society for the Promotion of Science) KAKENHI Grant number 21J22170, and Infotech Oulu.

* Corresponding author.

E-mail addresses: thi.tn.nguyen@oulu.fi (N. Nguyen), le.nguyen@oulu.fi (L. Nguyen), lihonghan@mbm.me.es.osaka-u.ac.jp (H. Li), miguel.bordallo@oulu.fi (M. Bordallo López), constantino.alvarezcasado@oulu.fi (C. Álvarez Casado).

<https://doi.org/10.1016/j.combiomed.2024.108873>

Received 25 April 2024; Received in revised form 5 July 2024; Accepted 8 July 2024

Available online 24 July 2024

0010-4825/© 2024 The Authors. Published by Elsevier Ltd. This is an open access article under the CC BY license (<http://creativecommons.org/licenses/by/4.0/>).

rPPG presents substantial challenges that can affect the accuracy of the extracted biosignals, thus affecting its viability as a core technology in other systems [1,11]. These challenges arise from a variety of factors inherent in video capture, but also in video data transmission. Major challenges in video-based rPPG include video codec distortions and image artifacts, which can affect the quality of the video signal and thereby the accuracy of rPPG measurements [1,12]. Issues such as noise and signal degradation, often due to poor recording conditions (low-light conditions) or problems during transmission, often accentuate these challenges [13,14]. Limitations in the dynamic range of cameras and video codecs complicate the detection of subtle skin color changes essential for accurate rPPG analysis [12,15]. Occlusions in video frames, such as those caused by movements, obstructive objects, facial accessories, or privacy anonymization methods can interrupt the extraction of blood volume pulse (BVP) signals from the face [16]. Lastly, hardware and network constraints, such as limited processing power and bandwidth, can degrade the performance of real-time data processing and transmission [14], crucial for applications like telemedicine and remote patient monitoring. These issues compromise the accuracy of vital sign measurements and limit the adaptability of rPPG in real-world scenarios. Addressing these challenges is imperative for advancing and broadening the use of rPPG technology [1,11].

This article provides an overview of rPPG technology, reviewing related research and outlining challenges in video-based applications. A systematic evaluation framework is introduced to assess how these challenges affect the quality of rPPG systems. Alongside this, potential solutions to tackle these challenges are proposed and validated through extensive testing on public databases. The paper concludes by discussing the implications of the findings, emphasizing the potential for improved remote vital sign monitoring, thereby providing engineers and researchers with informed insights for system design and integration into healthcare solutions. The contributions include:

- A comprehensive evaluation of rPPG signals extracted using both learning-based (specifically, deep learning) and non-learning-based (predominantly computer vision and signal processing) methods. This comparison assesses the effectiveness of each approach in managing artifacts, aiding in the identification of robust signal enhancement strategies.
- Quantifying the impact of spatial, temporal, and visual occlusion artifacts on rPPG signal quality, including intentional occlusions (anonymization), noise related to low-light conditions, color depth resolution, camera frame rate, stream resolution, and the impact of connectivity or computing resource limitations leading to random frame dropping.
- Proposing and evaluating denoising and inpainting strategies to improve rPPG accuracy in measuring HR in noisy and occluded conditions.
- A comparative evaluation of mitigation strategies to improve rPPG signals in the presence of computation and network-related issues.

These issues and mitigation strategies are evaluated across a broad selection of seven publicly available rPPG databases, as depicted in Table 1. This comprehensive evaluation encompasses a diverse range of scenarios, from typical static and resting scenarios to physical activities in gym settings and video call interactions.

2. Related work

rPPG is a non-invasive, contactless method that uses a video camera and ambient light to detect physiological signals by observing variations in skin color due to blood flow, reflecting the complex interactions of light with skin properties [1,24]. As light hits the skin, it reflects based on the angle of incidence and skin characteristics, including polarization, and then penetrates the skin, scattering when meeting skin

structures like cells and blood vessels. This process is influenced by skin chromophores like melanin and hemoglobin, which absorb specific light wavelengths. These changes in light intensity, recorded by the camera, correlate with the cardiac cycle; more light is absorbed during the systole when blood volume increases, and less during diastole. To improve signal detection accuracy, rPPG often employs green or near-infrared wavelengths, which hemoglobin preferentially absorbs.

However, the rPPG technology faces several intrinsic challenges. These are challenges inherent to the BVP signal capture process, tied to the immediate measurement environment and subject-specific factors such as motion artifacts due to subject movement [2], distance from the camera sensor to the skin area and resolution of the facial region [25], variations in skin pigmentation [26], environmental light conditions [27], or occlusions [16,28], either from external factors or from purposeful anonymization techniques [28]. All these factors can compromise the HR estimations [1]. Furthermore, extrinsic challenges are external conditions and technical limitations, mostly stemming from network and computing constraints that can significantly impact the performance of rPPG methods if not adequately addressed during development. These challenges, arising during video capture, processing, and transmission, include bandwidth limitations, packet loss, latency, video compression artifacts, frame rate variability, low resolution, camera sensor's rolling shutter effects, and restricted computational resources. Such factors can substantially degrade video quality, affecting the detection of subtle skin color variations which are crucial for accurate rPPG signal extraction and subsequent analysis [14,29–31]. This article studies how spatial factors (image resolution, color depth, blurring, and noise), occlusion (sunglasses and facemask), and temporal variation of frame rates influence the quality of rPPG signals. Compared to related work (see Table 2), the proposed evaluation framework thoroughly investigates these aspects of learning-based and non-learning rPPG methods. Furthermore, corresponding mitigation strategies are presented to improve the quality of extracted vital signs.

2.1. Intrinsic challenges

To address these challenges, studies have concentrated on enhancing rPPGs resilience to motion, adapting to skin tone variations, or improving signal quality amid noise and changes in illumination [2]. Traditional non-learning (NL)-based methodologies in rPPG have been extensively directed toward addressing physical artifacts by employing sophisticated models of light reflection, signal processing techniques, and BVP extraction from various color channels. Research efforts have largely aimed at isolating BVP signals from raw RGB video data using a variety of mathematical models and algorithms. Notably, techniques such as POS, CHROM, OMIT, LGI, CK, BSS, and ICA have been developed to isolate the pulsatile component of blood volume from the skin reflections recorded in RGB channels [2,3,32]. Among the earliest approaches, the GREEN method [33], proposed in 2008, utilizes the green video channel, which has been found to capture a stronger pulsatile signal relative to the red and blue channels [34]. To address motion artifacts, subsequent research has introduced strategies for stabilizing the region of interest, particularly focused in faces, using optical flow techniques and tracking algorithms [35,36]. Efforts to counteract the effects of head and facial movements have led to the development of face tracking and alignment approaches [2]. Additionally, several filtering approaches, including bandpass, adaptive, detrending, and LSTM-based filters, have been utilized to clean PPG signals from noise and motion-related disturbances [36–38]. Signal separation methods based on independent component analysis or blind source separation, such as PCA [39], CK [25], OMIT [2] or ICA [40], have been utilized to isolate the genuine physiological signals from uncorrelated signals and noise. Reflective models like CHROM [41] and POS [42] have been developed to separate the specular and diffuse reflection components, containing the pulsatile physiological signals. Approaches like [43,44] have focused on correlating signals using normalized

Table 1
Summary of databases used in the benchmark evaluation.

Database name	Abbreviation
COHFACE [17]	COHFACE
Local Group Invariance - Photoplethysmography Imaging [18]	LGI-PPGI
Multimodal Analysis of Human Nonverbal Behavior - Human Computer Interaction [19]	MAHNOB-HCI
Pulse Rate Detection Dataset [20]	PURE
Univ. Bourgogne Franche-Comté Remote PhotoPlethysmoGraphy [21]	UBFC-rPPG
University of California, Los Angeles - rPPG [22]	UCLA-rPPG
Univ. Bourgogne Franche-Comté - Physiology [23]	UBFC-Phys

Table 2
Comparison to related studies addressing challenging scenarios and factors that can affect the performance of rPPG systems.

Articles	Year	Spatial factors	Visual occlusion	Temporal variation
Yue et al. [31]	2021	✓		
Speth et al. [28]	2022		✓	
Nguyen et al. [16]	2023	✓	✓	
Álvarez Casado et al. [14]	2023			✓
This article	2024	✓	✓	✓

reference waveforms or noise reference signals, while others have concentrated on addressing illumination variations [43,45] and skin tone variations [46] to enhance the signal quality further. Exploring RGB channels further, the GRGB rPPG method [47] utilizes green-to-red (GR) and green-to-blue (GB) ratios, and their sum (GR + GB), to improve rPPG signal quality efficiently.

Deep learning (DL) and other learning-based approaches in rPPG have emerged in recent years to tackle intrinsic artifacts by learning physical reflective and absorption models for BVP in a data-driven manner. These methods offer automated solutions for issues like noise, movements, illumination changes, or video quality, enhancing HR estimation accuracy. Key developments include HR-CNN [48], an end-to-end two-step CNN, comprised of an extractor trained to optimize SNR for rPPG signal extraction from video frames, and an HR estimator that minimizes the mean absolute error (MAE) between predicted and ground-truth (GT) HR values, and DeepPhys [49], which utilizes deep networks with attention mechanisms and skin reflection models for signal extraction. RhythmNet [50] employs spatial-temporal mapping for continuous HR measurement, while [30] introduces a two-stage approach, combining video enhancement and 3D-CNN for rPPG signal recovery. Further innovations are seen in AutoHR [51], utilizing Neural Architecture Search for optimal signal extraction, and MetaRPPG [52], a transductive meta-learner for self-supervised learning. PulseGAN [53] represents a hybrid method combining unsupervised PPG extraction with a GAN for realistic pulse signal generation. The recent AND-rPPG [54] focuses on using Action Units and Temporal Convolutional Networks for effective signal denoising. Recent developments in supervised DL have significantly improved physiological signal estimation. MTTs-CAN [55] is a multi-task variant, halves computational costs, and facilitates information sharing between blood volume pulse and respiration signal estimation. Additionally, PhysFormer [56] offers an end-to-end video transformer architecture for remote physiological measurement, leveraging cascaded temporal difference transformer blocks and supervision in the frequency domain. EfficientPhys [57] introduces two new neural architectures, a visual transformer, and a convolutional network, marking the debut of visual transformers in camera-based physiological measurement and an end-to-end on-device neural architecture for mobile devices. In unsupervised DL, Gideon et al. [58] pioneer label-free rPPG estimation using a contrastive framework and robust loss functions. SiNC [59] leverages weak periodicity assumptions for accurate rPPG regression from unlabeled face videos, enabling camera-based vital sign measurements without GT data. Contrast-Phys [60] introduces a method trainable in unsupervised settings, leveraging spatiotemporal contrast for accurate rPPG measurement, robust against noise interference, and computationally efficient. Recently, bioinspired deep learning models that use human-like gaze behaviors and active learning [61] can enhance the robustness of rPPG

systems, improving physiological signal detection under challenging conditions.

Traditional NL-based rPPG methods excel in generalizing across different conditions without specific training data but face challenges with noise sensitivity and varying skin types. On the other hand, learning-based methods offer high accuracy and effective noise handling. These methods usually need minimal intervention beyond essential preprocessing, and they learn to recognize facial noise patterns in relation to GT PPG signals [62]. However, their dependency on representative training data restricts their generalizability and raises concerns about data acquisition costs and computational resources. Additionally, they often function as ‘black-box’ models with limited transparency, a significant drawback in healthcare applications [63].

2.2. Extrinsic challenges

Extrinsic factors, especially those related to network and computational constraints, can significantly impact the performance of rPPG systems [14], but this influence is often not fully considered in research. Not many studies have focused on this aspect. In the process of designing and implementing rPPG methods, many researchers assume ideal operating conditions, overlooking the complexities of deploying these systems in real-world environments, especially for real-time applications. This gap becomes particularly relevant in video streaming for real-time vital sign monitoring, where maintaining signal quality with low latency and limited bandwidth is crucial. Even with 5G and 6G advancements, suboptimal network conditions still occur, impacting rPPG performance. For instance, robust collaborative-relay beamforming techniques can mitigate video artifacts and network constraints, ensuring reliable real-time vital sign monitoring on wireless devices like smartphones and laptops [64]. Despite these advancements, external factors such as network or hardware limitations still need to be considered, as they can affect the performance of rPPG systems.

The main extrinsic factors impacting rPPG systems include video compression artifacts, frame rate variability, network jittering, and resolution adjustments. These can compromise the integrity of rPPG signals. Video compression may add noise and alter the time-based patterns essential for extracting accurate BVP signals [30,65,66]. Likewise, changes in frame rate and resolution can modify the signal’s morphological and frequency attributes, affecting the accuracy of physiological signal detection across different network conditions [14].

Some research studies have demonstrated that video compression may induce minor degradation in signal quality, affecting the features and morphology of the rPPG signal [12,15,65,67]. To address video compression artifacts, techniques including image filtering and DL-based methods have been proposed [30,65]. Singular spectrum analysis for signal reconstruction and selection has also been explored [66].

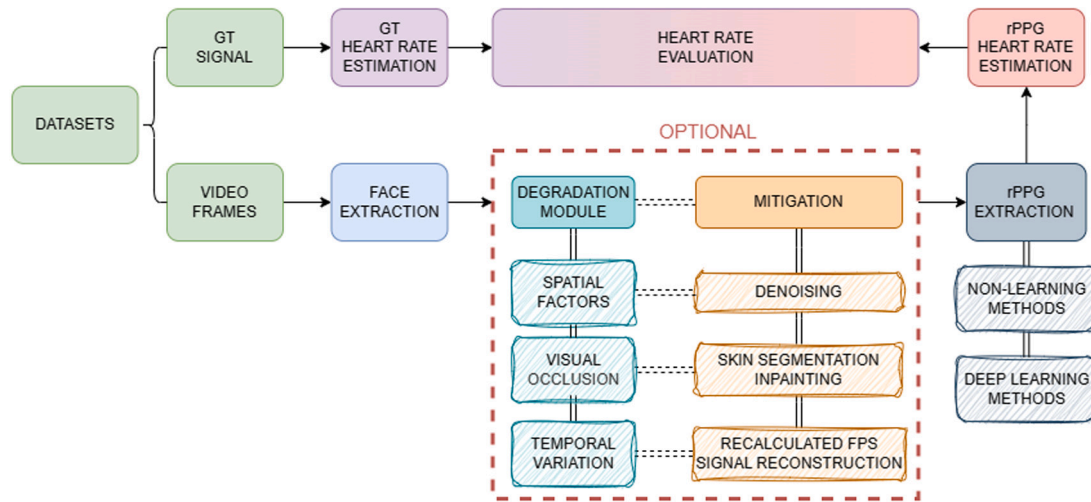


Fig. 1. Evaluation framework.

Studies on the effect of frame rate and image resolution suggest that maintaining typical values between 15 and 200 frames per second (fps) does not significantly impact HR estimation accuracy [68,69]. Efficient PPG signal coding strategies have been studied, but these require specific learning approaches and architecture [70]. Other studies have explored the effect of different image formats in DL-based rPPG approaches [71]. For example, Álvarez et al. [14] have conducted an in-depth analysis of the effects associated with regular and random frame dropping, as well as frame jittering, phenomena typically encountered during video calls. The study proposes several strategies to mitigate their detrimental impact on signal integrity. Additionally, Nguyen et al. [16] investigated the impact of noise on the performance of rPPG systems, both NL-based and learning-based, and have proposed denoising techniques to alleviate its adverse effects. Although these are clear steps to characterize these effects properly, further investigation is needed to fully understand and address other extrinsic factors like latency, packet loss, and computing resource limitations.

3. Evaluation framework

For the evaluation of rPPGs in challenging environments, a framework is proposed that integrates two optional modules into typically standard rPPG pipelines. These modules are designed to simulate potential degradation artifacts and implement corresponding mitigation strategies respectively. A simplified view of the proposed framework is depicted in Fig. 1.

Within a typical rPPG pipeline, the first step focuses on the capture and processing of video frames to detect the primary face in the input image. Subsequently, the degradation module introduces systematic spatial, temporal, and visual occlusion artifacts in the video frames. These controlled degradations aim to mimic real-world conditions, enabling the assessment of their effects on the rPPG signal extraction process. The module also allows the implementation of strategies that minimize the impact of these degradations on the performance of the rPPG techniques, improving resilience and real-world applicability. The assessment of rPPG methods may utilize either NL-based methods (predominantly signal processing) or learning-based approaches (mainly DL).

3.1. Datasets

The proposed evaluation framework includes seven datasets, as summarized in Table 3. These datasets offer a wide variety of input videos, captured under different conditions, including controlled

environments or natural settings, and in both compressed and uncompressed formats, for analyzing physiological signals and emotions. The reliability of the findings is ensured across different scenarios by examining multiple datasets.

COHFACE [17] contains video recordings of 40 subjects captured with a Logitech HD C525 webcam at 20 Hz, with a resolution of 640×480 pixels. The database comprises 160 videos, each lasting approximately 1 min. Reference physiological data was recorded using medical-grade equipment.

LGI-PPGI [18] features 24 videos of 6 users engaged in four scenarios: gym, resting, rotation, and talking, recorded at 640×480 pixels and 25 fps using a Logitech HD C270 webcam. Reference GT measurements are obtained using a CMS50E pulse oximeter device synchronized at 60 Hz.

MAHNOB-HCI or *MAHNOB* [19] is a multimodal database designed for emotion recognition, featuring 27 participants recorded with various cameras. The database includes 527 facial videos with corresponding reference physiological signals, recorded at 60 frames per second using an ECG sensor. In the evaluation of different experiments, only a curated subset of 81 videos from the MAHNOB database was utilized, inclusive of the first, middle, and last videos for each subject.

PURE [20] consists of videos of 10 subjects performing controlled head motions captured with an eco274CVGE camera at 30 Hz and a resolution of 640×480 pixels. The recording session involved six distinct setups, encompassing steady movements, talking, slow translation, fast translation, slow rotation, and medium rotation. Reference pulse data was collected using a pulox CMS50E fingertip pulse oximeter at a sampling rate of 60 Hz.

UBFC-rPPG 1 & 2 [21] contains 50 videos synchronized with a pulse oximeter finger-clip sensor, with lengths of approximately 2 min. Recorded at a frame rate of 28–30 Hz and a resolution of 640×480 pixels in uncompressed 8-bit RGB format.

UCLA-rPPG [22] includes 98 subjects with 4–5 videos per subject, recorded at 30 fps and lasting about 1 min each. A total of 488 videos were included, synchronized with GT HR data. To reduce redundancy in the dataset, only one video per subject was selected for analysis. Specifically, the second video from each subject was used, resulting in a total of 98 videos.

UBFC-Phys [23] comprises videos of 56 subjects recorded with an Edmund Optics EO-23121C RGB digital camera at 35 fps and a resolution of 1024×1024 pixels. Reference GT data were collected using an Empatica E4 wristband, including BVP, skin temperature, and

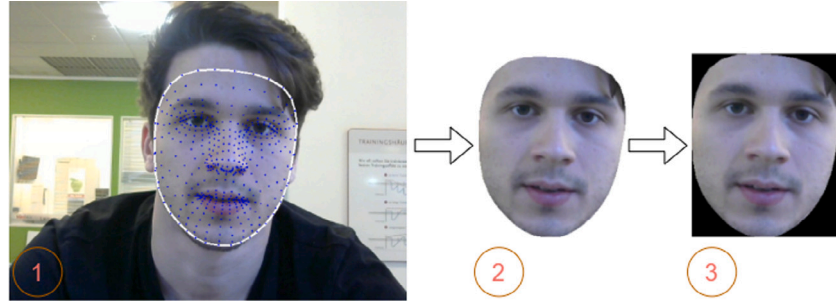


Fig. 2. Face extraction process in the rPPG evaluation pipeline. It involves three steps: (1) Landmarks detection, (2) Face segmentation, and (3) Background modification.

Table 3
Dataset specifications.

Dataset	Resolution	Video FPS	Reference signal sampling rate
COHFACE	640 × 480	20	256
LGI_PPGI	640 × 480	25	60
MAHNOB	780 × 580	61	256
PURE	640 × 480	30	60
UBFC1-rPPG	640 × 480	28	62
UBFC2-rPPG	640 × 480	23–29	30
UCLA-rPPG	640 × 480	30	30
UBFC-Phys	1024 × 1024	35	35

electrodermal activity responses. During the experiment, participants experienced social stress through a three-step process involving resting, speech, and arithmetic tasks.

3.2. Face detection and segmentation

In this study, the *MediaPipe* framework [72], a Google-powered machine learning solution for facial detection and segmentation from images and video streams, is used. The detection process operates by analyzing each frame individually to detect the face, as depicted in Fig. 2.

The detection process operates by analyzing each frame individually to detect and segment the face. It consists of two real-time deep neural network models that work together: A face detector, known as Blaze-Face from Google Research [73], that operates on the full image and computes face locations, and a 3D face landmark model that operates on those locations and predicts the approximate surface geometry via regression [74]. Using the *FACEMESH_FACE_OVAL* mode, MediaPipe constructs a segmentation mask based on the facial outline based on 468 3D face landmarks. Subsequently, this mask is applied to the original image to segment the desired face area, which is the region of interest to extract the BVP signals. To reduce noise, especially in signal processing-based rPPG methods, the background is changed to black pixels, as shown in Fig. 2. If the model fails to detect the face or its landmarks, face locations from previous frames where detection was successful are used.

3.3. rPPG extraction

rPPG extraction methods are categorized into two main groups: non-learning-based approaches and deep-learning-based techniques. Three non-learning-based methods (NLM) are selected: OMIT [2], which utilizes matrix decomposition to create an orthogonal RGB matrix and reconstructs the rPPG signal from the RGB signal using orthogonal components obtained through QR factorization; CHROM [41], which constructs orthogonal chrominance signals to mitigate specular reflections; and POS [42], which removes specular reflections using normalized RGB color space. Additionally, four deep learning methods (DLM) are included: EfficientPhys [57], which offers an end-to-end

solution with a customized normalization module, tensor-shift module, and hierarchical vision transformer architecture, trained on the UBFC-rPPG dataset [21]; ContrastPhys [60], which employs a 3DCNN model trained with a contrastive loss function on the UBFC-rPPG dataset [21]; PhysFormer [56], that utilize temporal difference transformer blocks for generating global-local rPPG features, trained on 1-fold of the VIPL-HR dataset [75] using a curriculum learning paradigm; and MTTS-CAN [55], which employs a multi-task temporal shift convolutional attention network for effective temporal modeling and signal source separation, with pre-trained models trained on the AFRL dataset [76].

While NL-based methods do not restrict input length, pre-trained DL methods often come with specific input size requirements (K) to be operational. Processing an entire video, composed of (N) frames, as input at once for DLM is usually not possible due to limited GPU and memory resources. Therefore, most methods call for dividing the video into M segments into specific lengths, where $M = \frac{N}{K}$ is advisable. If the last chunk contains a residual number of frames (R) smaller than the required input size (K) for DL models, frames from the previous chunk are used to pad it. In the experiments, preprocessing steps were conducted to align the data with the pre-trained data as closely as possible, using duplicate or extra frames in the input if required by the methods. Table 4 provides configuration details about the input and pre-trained models utilized in the study.

3.4. Heart rate estimation

After extracting the rPPG signal utilizing several rPPG methods and using the GT signal from datasets, the signals are segmented into distinct intervals using sliding windows of 10-s and 1-s steps (hence, 9-s overlap). Each signal window undergoes forward and backward filtering, configured as a bandpass filter within the range of 0.75 to 4 Hz (equivalent to 45–240 bpm).

Subsequently, HR estimation is performed using Welch's method with a specified nFFT value of 4096. This involves applying a Hamming window to each segment, with the length of each segment matching the length of the sliding signal window (n). Additionally, the number of points to overlap between segments is set to $\lfloor \frac{n}{8} \rfloor$, contributing to a robust and precise estimation of HR.

3.5. Evaluation metrics

To evaluate the accuracy of rPPG signals, the HR obtained from each rPPG window is compared to the HR from reference signals recorded simultaneously with the videos in the same window. This evaluation uses two well-known metrics: Mean Absolute Error (MAE) and Pearson Correlation Coefficient (PCC) of the heart-rate envelope.

MAE calculates the average absolute deviation between the predicted and GT HR envelopes. This calculation involves summing the absolute differences between the predicted values (\hat{y}_i) and the corresponding GT values (y_i) at each data point, and then averaging these differences across the entire dataset, as shown in Eq. (1).

$$\text{MAE} = \frac{1}{n} \sum_i^n |\hat{y}_i - y_i| \quad (1)$$

Table 4
Basic specifications for DLM.

DLM	Pretrained dataset	Chunk size	Input preprocessing
PhysFormer [56]	VIPL-HR	160	Image-Level normalization
ContrastPhys [60]	UBFC-rPPG	FPS \times 10	None
EfficientPhys [57]	UBFC-rPPG	FPS \times 10	Video-Level standardization
MTTS-CAN [55]	AFRL	320	Video-Level appearance and motion calculation

PCC measures the strength and direction of the linear relationship between the predicted and GT HR envelopes. It is calculated by comparing the covariance of the two signals to the product of their standard deviations, as shown in Eq. (2). Due to the anatomical variations in blood perfusion waveforms between the face and finger [2], the PCC between HR envelopes as a more appropriate evaluation metric, rather than comparing the waveforms directly. The main goal is to evaluate rPPG extraction methods under difficult conditions, rather than achieving waveform similarity with GT PPG signals.

$$\text{PCC} = \frac{\sum_i (\hat{y}_i - \hat{\mu})(y_i - \mu)}{\sqrt{\sum_i (\hat{y}_i - \hat{\mu})^2} \sqrt{\sum_i (y_i - \mu)^2}} \quad (2)$$

where \hat{y}_i is the predicted HR value in window i , $\hat{\mu}$ is the mean of the predicted values, y_i is the GT HR value in window i , and μ is the mean of GT values. The numerator represents the covariance between the predicted and GT values. The denominator is the product of their standard deviations.

Additionally, Peak Signal-to-Noise Ratio (PSNR) and Structural Similarity Index (SSIM) were used to evaluate the effectiveness of denoising and inpainting methods in improving image quality, as shown in Eqs. (3) and (4) respectively.

$$\text{PSNR}(f, g) = 10 \log_{10} \left(\frac{255^2}{\text{MSE}(f, g)} \right), \quad \text{where} \quad \text{MSE}(f, g) = \frac{1}{MN} \sum_{i=1}^M \sum_{j=1}^N (f_{ij} - g_{ij})^2 \quad (3)$$

$$\text{SSIM}(f, g) = l(f, g)c(f, g)s(f, g), \quad \text{where} \quad \begin{cases} l(f, g) = \frac{2\mu_f\mu_g + C_1}{\mu_f^2 + \mu_g^2 + C_1} \\ c(f, g) = \frac{2\sigma_f\sigma_g + C_2}{\sigma_f^2 + \sigma_g^2 + C_2} \\ s(f, g) = \frac{\sigma_{fg} + C_3}{\sigma_f\sigma_g + C_3} \end{cases} \quad (4)$$

In PSNR, f stands for the reference image, and g for the test image, both sized $M \times N$. For SSIM, $l(f, g)$ computes the similarity in mean luminance, $c(f, g)$ assesses the similarity in contrast using their standard deviations, and $s(f, g)$ measures the structural similarity by analyzing the correlation coefficient between them. Positive constants C_1 , C_2 , and C_3 are introduced to prevent division by zero.

4. Degradation module

The degradation module simulates a range of spatial factors, visual artifacts, and temporal variations to provide an extensive assessment under varied conditions. Spatial factors include changes in the size of the face crop and distortions due to head or camera movements, requiring stabilization techniques. These factors also account for variations in color bit depth. Visual artifacts simulate common occlusions, such as sunglasses and facemask, either alone or in combination. Temporal variations mimic fluctuations in video frame rates, reduced frame rates, or random frame dropping, indicative of network or processing lags in remote settings. This module is applied to the facial regions extracted across the entire dataset.

This simulation framework facilitates an in-depth evaluation of the evaluated rPPG methods, offering insights into the operational boundaries and capabilities of the technology across a range of unpredictable environments.

4.1. Spatial factors

These factors include differences caused by changing the input image size and the impact of alterations in the bit depth of the RGB image.

Facial region resolution. In NL rPPG methods, obtaining rPPGs typically revolves around obtaining RGB mean values extracted directly from skin areas of any size. However, employing pre-trained DL rPPG methods may impose stringent requirements about input requirements such as square image size or specific resolutions. Experiments are conducted at different facial region sizes using simple OpenCV resizing [77]. As a baseline, the 72×72 size was chosen due to its balance between computational efficiency and preservation of crucial facial information, as well as compatibility with the selected pre-trained DL models (see Fig. 3).

Color depth reduction. Variations in color bit depths in video streams result from a combination of factors, including the diversity of recording equipment, which ranges from smartphones to professional-grade cameras, each offering different levels of color detail. Video compression and encoding standards, such as H.264 and HEVC, further adjust these parameters to balance file size and quality, often reducing both resolution and color bit depth for efficient storage and transmission [78]. Bandwidth constraints during video streaming need these adjustments to ensure smooth delivery, with the video's resolution and color depth dynamically modified to fit network conditions and device capabilities. Adaptive streaming technologies like MPEG-DASH and Apple's HLS play a role here, optimizing video streams in real-time based on the viewer's internet speed and device performance. Additionally, user preferences for lower data consumption can lead to voluntary reductions in video quality. Such variations can be critical considerations in applications like rPPG, where accurate color information is key, demanding adaptive solutions to maintain signal accuracy across different video qualities. Existing rPPG datasets uniformly employ RGB-8 bit color channels, and mostly ignore the potential effects of reducing the color level depth. To simulate this effect, a straightforward mathematical operation is conducted to decrease the color depth of a video. Denoting each RGB-8 bit frame of the video as I and nb signifies the desired bit number, the operation is defined as follows:

$$I_{nb} = \left\lfloor \frac{I}{rf} \right\rfloor \cdot rf, \quad \text{where} \quad rf = \frac{2^8}{2^{nb}}, \quad \text{and} \quad nb \in \{6, 4, 2\} \quad (5)$$

This process involves determining a reduction factor rf based on the desired bit number and then applying floor division and multiplication to achieve the new color bit frame I_{nb} . Noteworthy are the values of I_{nb} still within the range of 0 to 255 similar to I . However, the distinction lies in the reduction of intensity levels from the original 2^8 to 2^{nb} for each respective channel. In this experiment, nb will take on values of 6, 4, and 2, as visually depicted in Fig. 4.

Facial image deterioration. Within image deterioration, the two most common types are blur and noise. The generation of these effects involves the utilization of Gaussian functions. Specifically, Gaussian blur is implemented with a square kernel size of 25×25 pixels to induce blur, while Gaussian noise is introduced by applying a distribution with a mean of 0 and a variance of 0.004. Blur and noise are applied to the facial regions, as demonstrated in Fig. 5.

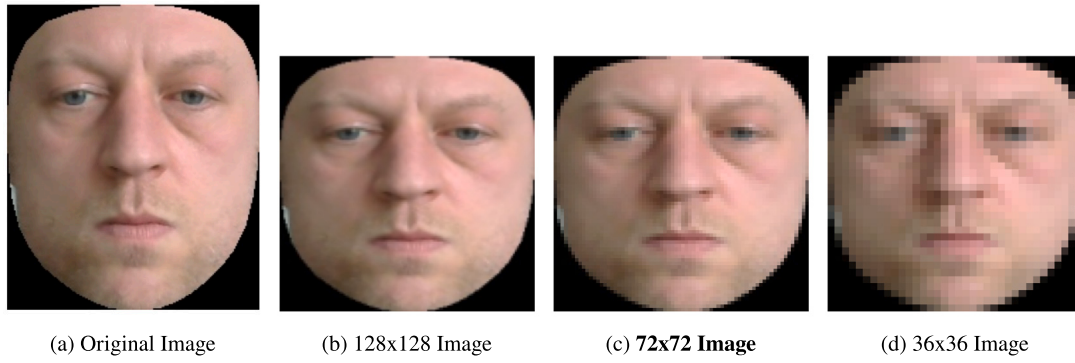


Fig. 3. Size variety of the face region.

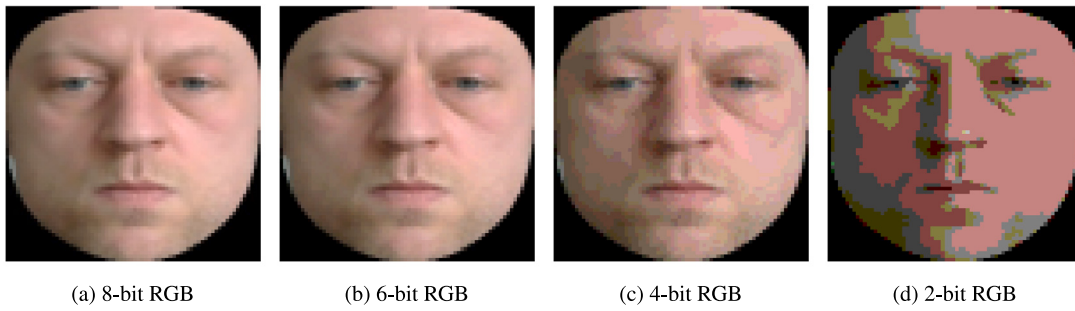


Fig. 4. Color depth reduction.

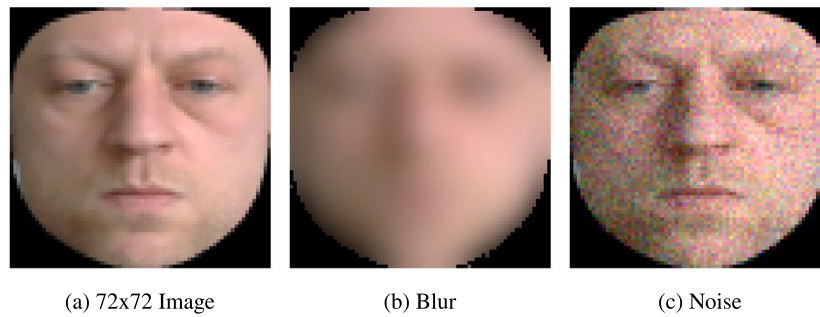


Fig. 5. Facial image deterioration under blur or noise.

4.2. Visual occlusion

Integrating HR monitoring into real-world scenarios must account for occlusions due to everyday items. Leveraging common accessories like facemask and sunglasses may result in heightened user adoption and sustained monitoring, particularly in outdoor or social settings. The experiments focus on two commonly worn items specifically, a white facemask and black sunglasses as illustrated in Fig. 6. The primary objective is to investigate the feasibility of maintaining the original performance of HR estimation when these objects cover an individual's face.

The process of integrating sunglasses into facial images involves several steps to ensure a seamless fit and alignment. Initially, the sunglasses undergo resizing to match the dimensions of the target face image. Following this, a translation is performed based on the midpoint of the resized sunglasses and the 6th landmark of the nose bridge, ensuring proper positioning. Subsequently, the sunglasses are aligned with the eyes, providing a natural and integrated appearance of sunglasses on the facial image.

The process of applying facemask follows a similar procedure. A mask image was designed based on 22 fiducial landmarks of the face

delineating the chin and the nose bridge landmark. Subsequently, the same corresponding set of 22 points on the face serves as destination points, outlining the boundary where the mask will be applied. Through the computation of a homography matrix utilizing the destination and source points, the function determines the transformation necessary to accurately map the mask onto the facial landmarks. This transformation, typically involving perspective warping, ensures seamless alignment of the mask with the facial features.

4.3. Temporal variation

Various devices and video capture systems often function at different frame rates. Also, in real-world applications, data may encounter sporadic sample dropping, attributed to network or computing limitations. In the experiments, HR computations were conducted at different frame rates. Since the original datasets have framerates of either 30 or 25 FPS, experiments were performed at the original rate along with deliberately reduced rates of 20 FPS, 15 FPS, and 10 FPS. The new rates were computed by simply dropping frames at the needed regular rate. In addition, simulated random frame drops into the video streams are introduced to replicate challenges commonly encountered

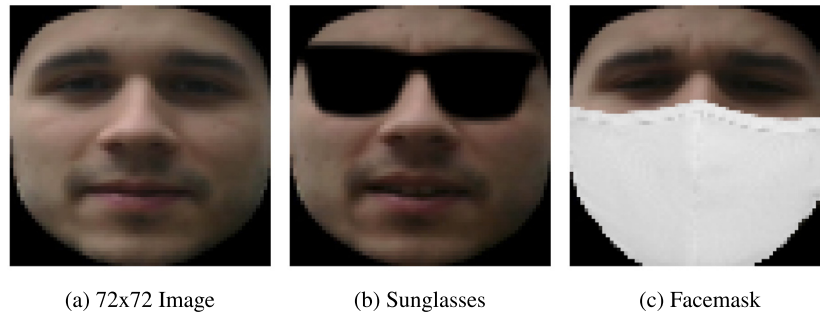


Fig. 6. Visual occlusion illustration.

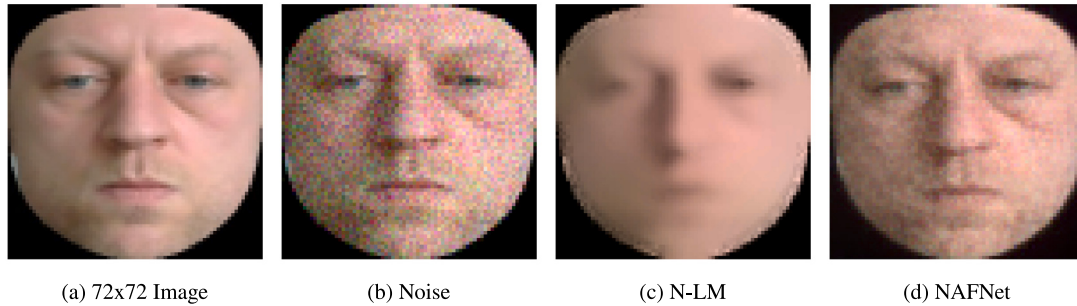


Fig. 7. Denoising illustration.

in transmission networks, including package loss, delay, and jitter, which can adversely impact real-time communication applications like video calls. HR calculations were then performed across a spectrum of random frame-drop rates, encompassing dropping 10%, 20%, and 50% of the total video frames.

5. Mitigation strategy

Although the impact of spatial and temporal deterioration cannot be fully mitigated, this study introduces and assesses a range of mitigation strategies specifically designed to address the most significant effects on both spatial (noise and occlusions) and temporal (random frame dropping) artifacts.

5.1. Noise mitigation

In this study, two denoising methods are utilized: Non-local Means (N-LM), an NL-based approach [79], and Nonlinear Activation Free Network (NAFNet), a DL technique [80].

The N-LM algorithm is a denoising technique leveraging natural image statistics to reduce noise, assuming that similar image patches exhibit comparable noise characteristics. The implementation provided by OpenCV (*fastNlMeansDenoisingColored*) was utilized, with the following parameters: a filter strength of 15 for both the luminance and color components, a template patch size of 7 pixels for weight computation, and a window size of 21 pixels for computing the weighted average for a given pixel.

The NAFNet model is a DL network with exceptional performance in denoising, deblurring, and super-resolution tasks. Developed by customizing a U-net architecture [81] with skip connections, this pre-trained 32-layer NAFNet on SIDD dataset [82] was used to assess its effectiveness in denoising datasets used for HR estimation. Notably, the key distinction is that denoising is now exclusively targeted at the face rather than the face with the background. This adjustment allows for a more focused investigation into the impact of noise on skin color, providing valuable insights into the denoising efficacy within this specific context. Fig. 7 illustrates an example of denoising utilizing these two methods.

5.2. Visual occlusion mitigation

Two strategies are proposed to mitigate the impact of occlusion on facial regions. The first method (OS) involves eliminating the facemask and sunglasses replacing them with black color, then only using the skin region of the face as shown in the first step of Fig. 8 for rPPG extraction.

The second method (GC) employs a Generative Adversarial Network (GAN) architecture to generate missing parts of the face and ensure accurate skin color of the generative skin region through color transfer. The GAN comprises a U-Net neural network as the generator, featuring a dual-path design with contracting and expansive paths. The discriminator, modeled after the WGAN-GP architecture, employs a unique loss function and gradient penalty to provide continuous feedback, ensuring detailed and realistic generated facial features. A facial dataset subset from FFHQ [83] was utilized for GAN training by applying sunglasses and facemask. The network underwent 100 epochs with a batch size of 16, a fixed learning rate of 2×10^{-4} for the generator and 1×10^{-4} for the discriminator, and the Adam optimizer for gradient descent optimization. Following that, the color transfer method is utilized to transfer the color from real skin regions to generated skin regions by leveraging the Lab* color space and the mean and standard deviation of each L*, a*, and b* channel. Fig. 8 illustrates each stage process of the methods applied to facial images in each type of face occlusion.

5.3. Random frame dropping mitigation

Two distinct mitigation strategies are implemented and evaluated to counteract the impact of these random frame drops. These strategies are intended for networked operations in which videos are transmitted over the network, involving both the receiver computing device and the transmitter computing device. The first strategy involves only the receiver, which recalculates the FPS for the current window based on the number of samples within the window length. The second strategy employs a collaborative approach between both the receiver and the transmitter, where each frame is timestamped and sent to the receiver, which then uses the timestamps to reconstruct the signal by

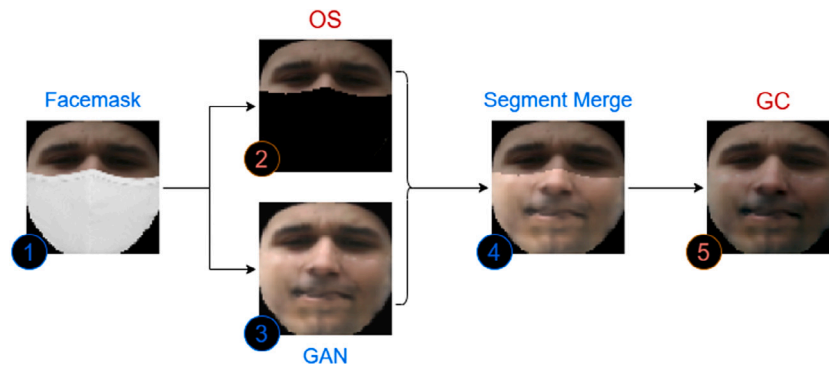


Fig. 8. Illustrations demonstrating facemask visual occlusion mitigation. (1) Facemask image, (2) Original skin image, (3) GAN generated image, (4) Merged image of original and generated skin, (5) Merged image with color transfer from real to generated skin.

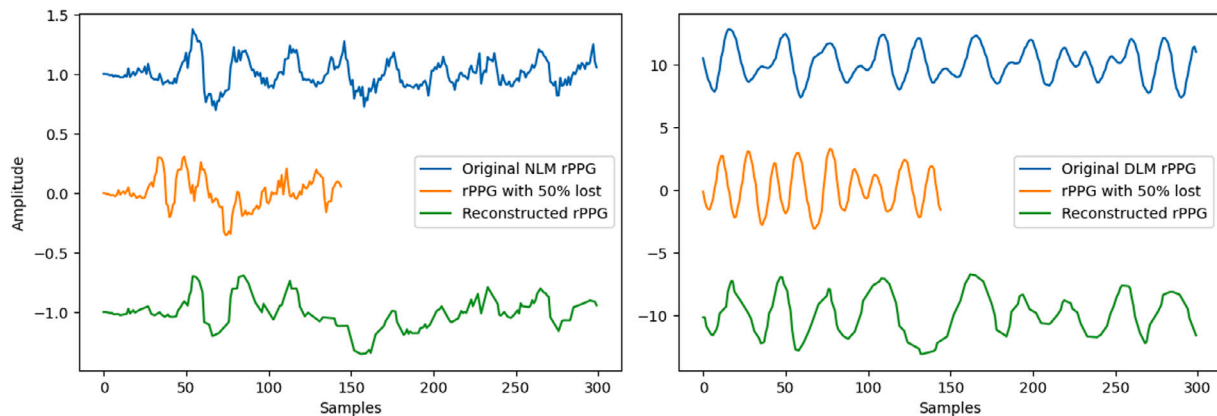


Fig. 9. rPPG Signals in 10 s: NL vs. DL with 50% frame drop and reconstruction (Signals vertically shifted for visual clarity).

either repeating the preceding valid frame, interpolating or inserting zeros and re-filtering to handle missing frames. In this research, one-dimensional linear interpolation is employed to reconstruct the signal. Fig. 9 depicts 10 s rPPG signals before and after randomly dropping 50% of frames, alongside the reconstructed signal, using both NLM and DLM.

6. Results

Experiments are conducted on both the impact of spatial and temporal degradations and the proposed mitigation experiments in seven different datasets, comparing them with baseline results.

6.1. Impact of the spatial factors

Although the research dataset inputs deviate from the precise training conditions of DLM, a comparison was conducted to assess the adaptability of pre-trained models in handling slightly different input types for the same specific task. Notably, the NLM is expected to compete or even outperform DLM, due to the discrepancy between training and testing data.

The experiments are summarized in Table 5, which shows the performance across a range of different facial region sizes. Based on the results a size of 72×72 was selected for subsequent experiments due to its balanced performance across both NLM and DLM. This size proved suitable for deployment on EfficientPhys and ContrastPhys, yielding competitive results across diverse datasets while striking a commendable balance between accuracy and resource requirements.

While some rPPG methods showed marginal improvements on specific datasets at particular sizes, the experimentation on size variations revealed minimal impact on HR estimation in the NLM. In the DLM, the

ContrastPhys model exhibited notable flexibility in handling input size variations, offering greater experimentation opportunities compared to models reliant on fixed dataset sizes. However, it is worth noting that the model still requires uniform input sizes, presenting challenges with original extracted images of varying dimensions. The MTTS-CAN model, designed for pulse and respiration estimation, demonstrated comparatively suboptimal performance in the research, potentially due to distinct dataset processing methods.

Among all the datasets the MAHNOB dataset presents a formidable challenge across various rPPG methods and image sizes. This challenge likely stems from the dataset's inherent complexity, which encompasses diverse emotional expressions, varying lighting conditions, facial movements, and GT derived from brain signals.

6.1.1. Experiments on color depth reduction

Different methods are compared using frames with varying color depths. Table 6 illustrates a consistent trend observed across most datasets, indicating a general decrease in HR estimation as the bit depth decreases. The results consistently favor the use of 8-bit color depth, yielding the most favorable outcomes, while the 2-bit color depth consistently produces the lowest results.

Remarkably, 6-bit depth yields results that are almost as good as those from standard 8-bit images suggesting that there might be room for optimization or compression in image processing pipelines without sacrificing significant accuracy in HR estimation. This insight could be particularly valuable in resource-constrained environments, such as mobile or wearable devices, where reducing the bit depth can lead to substantial savings in memory and processing power.

Additionally, it is noteworthy that the EfficientPhys method appears to be particularly sensitive to decreasing bit depth, as evidenced by the more pronounced impact observed in its performance.

Table 5
Various image sizes in HR estimation.

Size	rPPG Meth.	Dataset													
		COHFACE		LGI-PPGI		MAHNOB		PURE		UBFC-rPPG		UCLA-rPPG		UBFC-Phys	
		MAE	PCC	MAE	PCC	MAE	PCC	MAE	PCC	MAE	PCC	MAE	PCC	MAE	PCC
NLM															
Org	OMIT	11.33	0.26	8.73	0.73	36.87	0.02	1.41	0.98	3.46	0.95	3.59	0.57	13.31	0.27
128		11.28	0.26	8.76	0.73	36.94	0.03	1.41	0.98	3.45	0.95	3.59	0.57	13.30	0.27
72		11.24	0.27	8.79	0.73	36.93	0.02	1.43	0.98	3.49	0.94	3.65	0.56	13.30	0.27
36		11.37	0.26	8.83	0.73	36.82	0.02	1.42	0.98	3.47	0.94	3.68	0.56	13.32	0.27
Org	CHROM	12.29	0.20	10.73	0.60	36.98	0.00	1.33	0.98	3.06	0.97	3.70	0.59	13.63	0.25
128		12.36	0.20	10.85	0.60	36.95	−0.01	1.35	0.98	3.06	0.97	3.69	0.59	13.63	0.25
72		12.39	0.21	10.87	0.60	37.13	−0.02	1.42	0.98	3.05	0.97	3.76	0.59	13.65	0.25
36		12.36	0.21	10.84	0.61	37.37	0.00	1.42	0.98	3.02	0.97	3.76	0.59	13.61	0.25
Org	POS	11.67	0.27	6.01	0.84	36.50	0.04	1.23	0.99	2.72	0.99	3.03	0.65	13.71	0.25
128		11.63	0.27	6.05	0.84	36.65	0.03	1.23	0.99	2.72	0.99	3.03	0.65	13.71	0.25
72		11.58	0.27	6.05	0.84	36.55	0.03	1.25	0.99	2.74	0.99	3.06	0.65	13.69	0.25
36		11.68	0.27	6.10	0.84	36.51	0.02	1.23	0.99	2.72	0.99	3.16	0.63	13.73	0.25
DLM															
Org	PhysFormer	–	–	–	–	–	–	–	–	–	–	–	–	–	–
128		12.47	0.03	17.26	0.48	44.13	−0.09	20.48	0.14	22.20	0.05	16.72	0.02	18.53	−0.04
72		–	–	–	–	–	–	–	–	–	–	–	–	–	–
36		–	–	–	–	–	–	–	–	–	–	–	–	–	–
Org	EfficientPhys	–	–	–	–	–	–	–	–	–	–	–	–	–	–
128		–	–	–	–	–	–	–	–	–	–	–	–	–	–
72		17.46	0.06	18.33	0.37	38.35	−0.03	10.12	0.50	7.73	0.69	7.99	0.37	15.93	0.17
36		–	–	–	–	–	–	–	–	–	–	–	–	–	–
Org	MTTS CAN	–	–	–	–	–	–	–	–	–	–	–	–	–	–
128		–	–	–	–	–	–	–	–	–	–	–	–	–	–
72		–	–	–	–	–	–	–	–	–	–	–	–	–	–
36		38.46	0.00	55.63	0.08	53.40	−0.14	89.80	0.06	71.09	0.09	100.07	0.03	83.09	0.00
Org	ContrastPhys	–	–	–	–	–	–	–	–	–	–	–	–	–	–
128		9.65	0.21	13.39	0.52	46.51	0.07	10.91	0.62	3.14	0.97	6.43	0.44	16.29	0.20
72		9.67	0.22	13.86	0.50	46.52	0.06	11.63	0.59	3.72	0.94	7.13	0.40	16.87	0.17
36		10.20	0.14	16.17	0.37	45.50	0.10	14.59	0.38	4.91	0.87	9.32	0.31	17.98	0.15

The bolded number serves as the baseline result (BS) for subsequent experiments, where the images are resized to a dimension of 72×72 pixels.

Table 6
HR estimation errors: Baseline & RGB bit reduction.

RGB	rPPG Meth.	Dataset													
		COHFACE		LGI-PPGI		MAHNOB		PURE		UBFC-rPPG		UCLA-rPPG		UBFC-Phys	
		MAE	PCC	MAE	PCC	MAE	PCC	MAE	PCC	MAE	PCC	MAE	PCC	MAE	PCC
NLM															
8 bit	OMIT	11.24	0.27	8.79	0.73	36.93	0.02	1.43	0.98	3.49	0.94	3.65	0.56	13.30	0.27
6 bit		11.54	0.27	8.93	0.72	37.21	0.00	1.40	0.98	3.54	0.94	3.55	0.59	13.35	0.27
4 bit		13.15	0.23	9.34	0.71	36.33	0.08	1.88	0.95	3.51	0.95	4.26	0.54	13.59	0.25
2 bit		19.01	0.16	13.82	0.56	37.09	0.03	6.85	0.70	16.44	0.38	9.62	0.38	15.63	0.20
8 bit	CHROM	12.39	0.21	10.87	0.60	37.13	−0.02	1.42	0.98	3.05	0.97	3.76	0.59	13.65	0.25
6 bit		12.42	0.22	10.85	0.61	37.42	−0.04	1.44	0.98	3.07	0.97	3.79	0.59	13.59	0.25
4 bit		14.76	0.16	11.70	0.57	36.40	0.05	2.08	0.94	3.09	0.97	4.47	0.54	13.87	0.23
2 bit		19.13	0.08	15.00	0.53	37.08	0.02	11.36	0.46	15.11	0.43	10.70	0.35	15.76	0.18
8 bit	POS	11.58	0.27	6.05	0.84	36.55	0.03	1.25	0.99	2.74	0.99	3.06	0.65	13.69	0.25
6 bit		11.81	0.29	5.97	0.84	37.00	0.01	1.23	0.99	2.78	0.98	3.09	0.65	13.70	0.25
4 bit		14.03	0.24	6.65	0.82	36.07	0.07	2.01	0.95	2.78	0.98	3.99	0.56	13.82	0.25
2 bit		22.01	0.17	13.47	0.59	36.89	0.01	12.84	0.46	14.31	0.44	9.89	0.39	15.69	0.20
DLM															
8 bit	EfficientPhys	17.46	0.06	18.33	0.37	38.35	−0.03	10.12	0.50	7.73	0.69	7.99	0.37	15.93	0.17
6 bit		17.50	0.05	18.46	0.38	37.96	−0.03	10.95	0.45	8.63	0.65	8.52	0.34	16.26	0.16
4 bit		17.92	0.07	20.17	0.32	37.61	0.03	16.08	0.23	14.92	0.42	12.34	0.18	18.24	0.07
2 bit		27.94	0.00	26.07	0.12	48.73	−0.01	26.34	−0.03	35.97	0.15	25.77	−0.02	22.39	0.03
8 bit	ContrastPhys	9.67	0.22	13.86	0.50	46.52	0.06	11.63	0.59	3.72	0.94	7.13	0.40	16.87	0.17
6 bit		9.66	0.22	13.78	0.51	46.60	0.05	11.84	0.58	3.73	0.94	7.28	0.40	16.94	0.17
4 bit		10.09	0.18	14.73	0.43	46.24	0.07	15.42	0.43	3.64	0.95	8.17	0.36	17.31	0.17
2 bit		11.28	0.05	16.34	0.39	43.89	0.05	26.37	0.22	10.05	0.63	12.43	0.27	18.80	0.13

The bold number represents the 8-bit RGB image at 72×72 pixels, reflecting the previous baseline result in Table 5.

Table 7

HR estimation errors: Baseline, deteriorated, and denoising datasets.

Type	rPPG Meth.	Dataset													
		COHFACE		LGI-PPGI		MAHNOB		PURE		UBFC-rPPG		UCLA-rPPG		UBFC-Phys	
		MAE	PCC	MAE	PCC	MAE	PCC	MAE	PCC	MAE	PCC	MAE	PCC	MAE	PCC
NLM															
BS	OMIT	11.24	0.27	8.79	0.73	36.93	0.02	1.43	0.98	3.49	0.94	3.65	0.56	13.30	0.27
Blur		11.45	0.25	8.82	0.72	36.99	0.02	1.42	0.98	3.45	0.95	3.53	0.58	13.30	0.28
Noise		41.58	0.10	17.10	0.50	44.83	0.02	17.62	0.35	13.62	0.54	20.16	0.27	18.81	0.19
NAFN		38.61	0.10	18.07	0.50	46.10	0.00	18.52	0.37	15.10	0.49	21.50	0.28	19.43	0.19
N-LM		42.68	0.11	18.54	0.49	45.31	0.05	17.41	0.36	14.87	0.51	22.26	0.24	19.65	0.20
BS	CHROM	12.39	0.21	10.87	0.60	37.13	−0.02	1.42	0.98	3.05	0.97	3.76	0.59	13.65	0.25
Blur		12.29	0.20	10.48	0.62	37.52	−0.04	1.40	0.98	3.04	0.97	3.70	0.59	13.59	0.25
Noise		48.04	0.09	19.90	0.42	46.24	0.02	19.58	0.33	17.12	0.44	19.85	0.28	19.49	0.20
NAFN		43.20	0.07	20.76	0.38	46.60	0.02	22.33	0.31	18.68	0.40	21.67	0.27	19.61	0.19
N-LM		50.58	0.10	20.96	0.40	47.43	0.02	19.98	0.33	18.70	0.42	21.35	0.26	20.12	0.19
BS	POS	11.58	0.27	6.05	0.84	36.55	0.03	1.25	0.99	2.74	0.99	3.06	0.65	13.69	0.25
Blur		11.82	0.25	5.87	0.85	36.50	0.03	1.23	0.99	2.76	0.98	3.08	0.64	13.67	0.25
Noise		42.75	0.10	16.50	0.54	44.55	0.03	18.30	0.35	13.00	0.53	21.44	0.27	19.67	0.20
NAFN		39.93	0.09	17.34	0.51	45.42	0.03	18.14	0.37	14.02	0.50	21.99	0.28	20.23	0.20
N-LM		43.94	0.09	17.76	0.51	44.83	0.05	18.69	0.33	14.01	0.50	23.22	0.24	20.39	0.21
DLM															
BS	EfficientPhys	17.46	0.06	18.33	0.37	38.35	−0.03	10.12	0.50	7.73	0.69	7.99	0.37	15.93	0.17
Blur		15.86	0.14	17.64	0.42	37.66	0.02	8.89	0.55	5.16	0.85	5.59	0.51	15.59	0.18
Noise		23.10	0.00	27.27	0.08	40.04	−0.04	27.07	−0.01	32.81	−0.02	26.06	0.05	23.60	−0.01
NAFN		22.35	−0.01	25.13	0.13	37.71	−0.03	22.40	0.03	29.90	0.04	19.54	0.04	22.30	0.01
N-LM		20.46	0.06	25.44	0.12	39.24	0.03	23.84	0.07	28.79	0.10	20.81	0.03	22.46	0.02
BS	ContrastPhys	9.67	0.22	13.86	0.50	46.52	0.06	11.63	0.59	3.72	0.94	7.13	0.40	16.87	0.17
Blur		9.44	0.26	13.75	0.51	46.90	0.07	11.89	0.59	3.65	0.94	6.81	0.42	17.45	0.17
Noise		10.10	0.10	14.06	0.51	46.58	0.08	26.31	0.16	6.11	0.81	15.11	0.17	21.33	0.07
NAFN		10.54	0.08	15.30	0.43	45.37	0.07	26.36	0.16	7.18	0.75	16.85	0.13	22.82	0.05
N-LM		10.26	0.14	14.78	0.47	46.36	0.08	25.05	0.21	7.02	0.75	15.10	0.15	22.36	0.06

The term BS represents the normal image at 72×72 pixels, the bold represents the deteriorated result needing improvement, while the underline marks enhancements in both metrics compared to the bold.

6.1.2. Experiments on image degradation and mitigation strategies

Experiments were conducted for different image degradation and mitigation strategies. To address the degradation caused by noise, two denoising methods, NAFNet and N-LM, were applied, and a summary of all results is presented in Table 7.

The results underscore the impact of degradation techniques, such as blurring and noise, on the performance of HR estimation methods. Notably, blur tends to have a mild impact, and in certain methods and datasets, a blur effect can even slightly enhance performance. Conversely, noise consistently exerts a more pronounced effect on performance.

When considering deteriorated factors in HR estimation across datasets like COHFACE, LGI-PPGI, UBFC-rPPG, and UCLA-rPPG, the ContrastPhys method demonstrates lower susceptibility to noise compared to other methods, particularly those in NLM. Although EfficientPhys exhibits relatively lower noise susceptibility in the COHFACE dataset compared to NLM, its performance is significantly affected in other datasets, especially in UBFC-rPPG where it has been pre-trained. Despite these variations, NLM consistently outperform DLM across various degradation types and datasets, except in COHFACE noise datasets, showcasing their robustness. However, DLM demonstrate notable resilience to noise, particularly exemplified by ContrastPhys.

Regarding denoising, while NAFNet and N-LM contribute to improved image quality, the corresponding enhancement in HR estimation performance is not as pronounced as shown in Table 7. For NLM, the denoising strategies fail to demonstrate significant improvement with N-LM in most datasets, with only NAFNet's denoising method showing slight improvement in COHFACE in terms of the MAE metric. For DLM, in the case of EfficientPhys, both NAFNet and N-LM denoising strategies yield marginal performance improvement, while ContrastPhys does not exhibit any improvement despite the application of denoising techniques.

In addition to the impact on HR estimation, Fig. 10 presents an average of all datasets and provides a comparative assessment of image

quality metrics, including PSNR and SSIM, where higher values generally indicate superior image quality. Notably, the figure demonstrates that noise and blur deteriorate image quality factors by 36%–37%. The N-LM and NAFNet methods respectively demonstrate an average improvement in image quality across both metrics, with SSIM increasing by 20%–25% and PSNR by 1.84–2.51.

6.2. Visual occlusion and mitigation

Experiments were conducted on visual occlusion and mitigation strategies based on inpainting, and the results are illustrated in Table 8.

These results show that the impact of sunglasses on performance for both DLM and NLM was minimal. This could be attributed to the fact that the black color of sunglasses has a lesser effect compared to other colors or eye regions that do not contain important signal information. Hence, mitigation strategies also had minimal impact.

However, the presence of a facemask significantly affects the accuracy of HR estimation, with some datasets and methods experiencing a two-fold decrease in accuracy compared to the original. Subsequently, for facemask, both mitigation strategies showed some mild improvements that varied across datasets and methods.

The original skin region approach exhibited improvement across most datasets and methods and seems to outperform the GC methods. This suggests that while the GC methods generate visually acceptable faces, they may lack certain information crucial for HR estimation, resulting in no improvement in accuracy.

However, the DLM demonstrated different trends. While ContrastPhys exhibited a slight improvement in some datasets with both mitigation methods, EfficientPhys performed poorly. This discrepancy may be attributed to the nature of the EfficientPhys model, which relies on temporal information, making the generated skin pixels lack the necessary temporal context. Additionally, the OS method only contains part of the skin region, resulting in a further decrease in performance due to the lack of essential skin pixels.

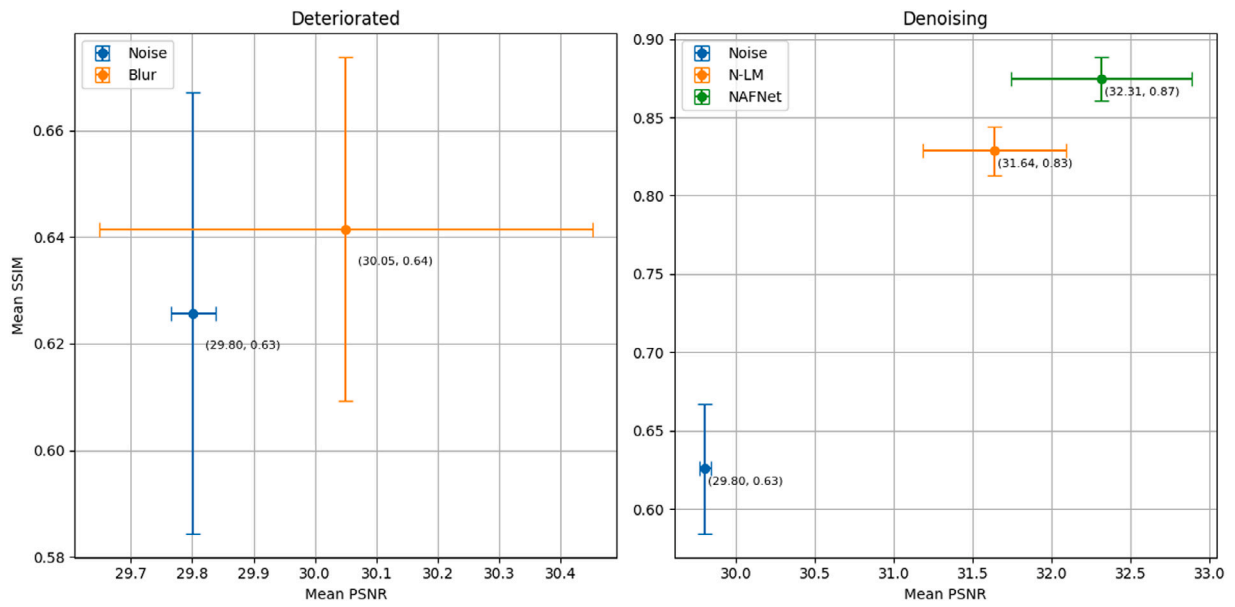


Fig. 10. Average image quality evaluation for deteriorated & mitigation.

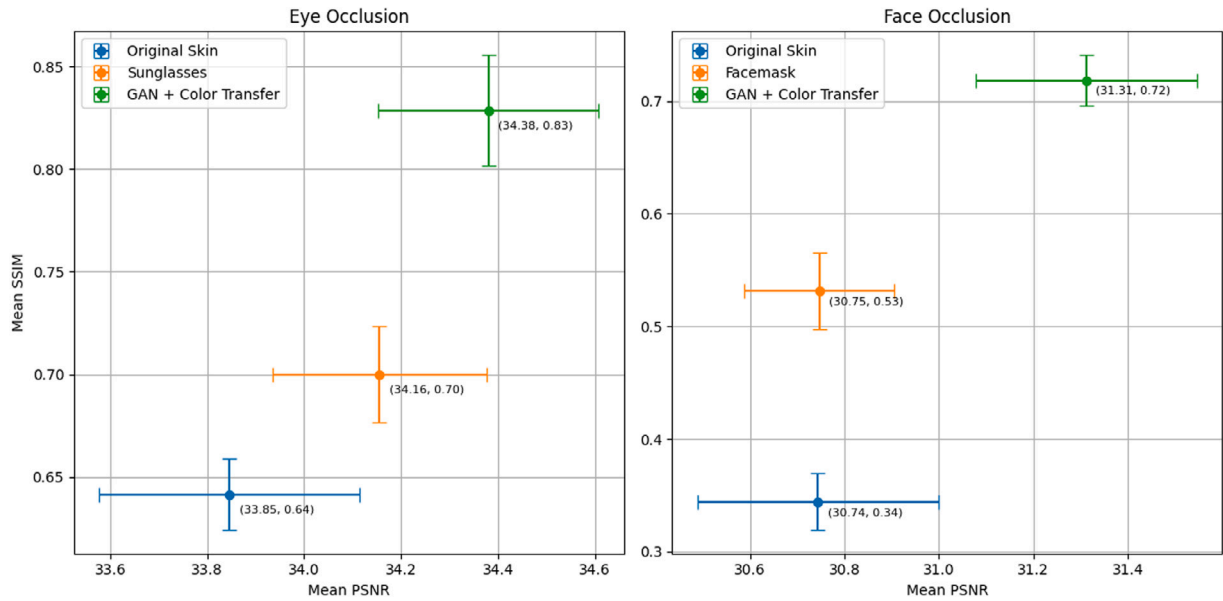


Fig. 11. Average image quality evaluation for occlusion & mitigation.

Results on image quality metrics are also computed and shown in Fig. 11, demonstrating an average of all datasets and providing a comparative assessment of image quality metrics. Notably, the figure demonstrates that sunglasses impact image quality by 26%–33%, while the facemask has a more significant impact, ranging from 41%–51%.

As expected, the first mitigation strategy (OS), which replaces occluded parts with a black background, consistently decreases image quality in all occlusion scenarios. Conversely, the second mitigation strategy (GC) proves to be the most effective in mitigating the impact of occlusions on image quality. Specifically, in scenarios where the face is occluded by a facemask region, the GC strategy improves SSIM by about 19% and PSNR by approximately 0.56. Similarly, when occluded by sunglasses, the GC strategy improves SSIM by about 13% and PSNR by approximately 0.22. These results show that image quality is important for visualization purposes, but might not necessarily result in better estimation of rPPG signals.

6.3. Temporal variation analysis

Experiments are conducted on both changes in sample rate and random frame dropping, which are shown in Table 9. In the experiments, the COHFACE dataset has an original frame rate of 20 FPS, resulting in one missing result compared to other datasets.

When simulating downsampled frame rates from the original down to 10 FPS, the results for NLM remain relatively consistent, with minor fluctuations across datasets. There are some unexpected improvements, but they are not substantial. However, with DLM, EfficientPhys exhibits unusual behavior, demonstrating better performance at lower frame rates in some datasets, even in its pre-trained UBFC-rPPG dataset with 30 FPS. This anomaly may be due to the lower frame rate providing more information on the differences between the two frames, which benefits the model, but requires a more in-depth investigation.

Table 8

HR estimation errors: Baseline, occlusion & mitigating datasets.

Types	rPPG Meth.	Dataset													
		COHFACE		LGI-PPGI		MAHNOB		PURE		UBFC-rPPG		UCLA-rPPG		UBFC-Phys	
		MAE	PCC	MAE	PCC	MAE	PCC	MAE	PCC	MAE	PCC	MAE	PCC	MAE	PCC
NLM															
BS	OMIT	11.24	0.27	8.79	0.73	36.93	0.02	1.43	0.98	3.49	0.94	3.65	0.56	13.30	0.27
SG		11.46	0.26	9.45	0.73	37.28	0.03	1.76	0.96	3.64	0.94	3.43	0.57	13.83	0.23
GC		12.96	0.21	9.94	0.70	37.39	0.04	2.23	0.94	4.22	0.90	4.11	0.50	14.18	0.22
OS		11.96	0.23	9.95	0.70	37.58	0.02	2.17	0.94	3.83	0.92	3.44	0.57	14.00	0.22
FM		21.89	0.05	10.76	0.69	36.86	0.03	2.99	0.89	10.53	0.48	7.01	0.43	15.47	0.20
GC		<u>19.47</u>	<u>0.07</u>	<u>9.86</u>	<u>0.70</u>	37.93	0.03	4.73	0.76	<u>5.84</u>	<u>0.69</u>	8.93	0.37	<u>14.06</u>	<u>0.26</u>
OS		<u>15.13</u>	<u>0.10</u>	<u>8.30</u>	<u>0.78</u>	<u>36.77</u>	<u>0.05</u>	<u>2.07</u>	<u>0.95</u>	<u>4.58</u>	<u>0.78</u>	7.38	0.39	<u>13.72</u>	<u>0.27</u>
BS	CHROM	12.39	0.21	10.87	0.60	37.13	-0.02	1.42	0.98	3.05	0.97	3.76	0.59	13.65	0.25
SG		12.67	0.19	11.43	0.61	37.50	0.01	1.75	0.96	3.92	0.89	3.79	0.55	14.04	0.23
GC		13.21	0.20	11.99	0.58	<u>37.34</u>	<u>0.03</u>	2.20	0.94	<u>3.57</u>	<u>0.93</u>	4.28	0.52	14.49	0.20
OS		12.68	0.21	11.39	0.61	<u>37.72</u>	0.00	1.85	0.96	<u>3.70</u>	<u>0.92</u>	3.80	0.57	14.18	0.22
FM		20.08	0.06	11.60	0.64	36.91	0.04	1.84	0.96	11.42	0.44	6.87	0.46	14.88	0.25
GC		19.32	0.06	<u>10.72</u>	<u>0.65</u>	38.17	0.00	4.68	0.76	<u>5.22</u>	<u>0.79</u>	7.97	0.41	<u>14.27</u>	<u>0.26</u>
OS		<u>15.46</u>	<u>0.11</u>	<u>9.86</u>	<u>0.69</u>	36.67	0.03	1.86	0.95	<u>4.11</u>	<u>0.85</u>	6.84	0.42	<u>13.81</u>	<u>0.27</u>
BS	POS	11.58	0.27	6.05	0.84	36.55	0.03	1.25	0.99	2.74	0.99	3.06	0.65	13.69	0.25
SG		12.10	0.26	5.85	0.86	36.99	0.03	1.69	0.97	2.90	0.97	3.15	0.61	14.00	0.23
GC		13.88	0.21	6.85	0.82	36.94	0.03	1.80	0.97	3.19	0.96	3.90	0.52	14.37	0.21
OS		12.59	0.24	<u>5.81</u>	<u>0.88</u>	37.30	0.00	1.76	0.97	3.03	0.97	3.26	0.58	14.08	0.23
FM		17.98	0.07	7.74	0.79	36.57	0.02	2.04	0.95	4.72	0.83	6.84	0.38	14.46	0.23
GC		21.58	0.09	9.20	0.73	37.79	0.04	5.26	0.70	<u>3.64</u>	<u>0.92</u>	8.77	0.36	<u>14.18</u>	<u>0.26</u>
OS		<u>16.04</u>	<u>0.11</u>	<u>7.07</u>	<u>0.81</u>	36.60	0.03	2.00	0.95	<u>2.91</u>	<u>0.98</u>	7.26	0.37	<u>13.71</u>	<u>0.27</u>
DLM															
BS	EP	17.46	0.06	18.33	0.37	38.35	-0.03	10.12	0.50	7.73	0.69	7.99	0.37	15.93	0.17
SG		17.77	0.06	19.86	0.36	39.10	-0.05	13.06	0.36	14.42	0.40	9.81	0.28	16.61	0.16
GC		18.56	0.04	20.25	0.35	<u>38.31</u>	<u>0.02</u>	14.05	0.32	15.56	0.37	10.70	0.26	17.01	0.15
OS		18.31	0.04	<u>19.23</u>	<u>0.38</u>	<u>38.82</u>	<u>0.01</u>	14.25	0.29	14.38	0.39	10.88	0.24	16.58	0.15
FM		21.65	-0.01	24.40	0.15	39.22	0.00	22.74	0.05	30.68	-0.05	21.06	0.02	22.85	0.00
GC		21.18	-0.01	<u>23.09</u>	<u>0.26</u>	38.12	0.00	<u>22.61</u>	<u>0.08</u>	<u>29.86</u>	<u>0.02</u>	21.05	0.00	22.26	0.00
OS		<u>39.90</u>	<u>0.04</u>	43.12	0.06	50.80	-0.09	58.43	0.03	54.67	0.18	70.32	0.08	39.33	0.03
BS	CP	9.67	0.22	13.86	0.50	46.52	0.06	11.63	0.59	3.72	0.94	7.13	0.40	16.87	0.17
SG		9.97	0.16	16.44	0.36	45.66	0.06	14.99	0.44	3.69	0.93	8.41	0.36	18.95	0.13
GC		10.31	0.16	<u>14.87</u>	<u>0.47</u>	47.41	0.06	18.02	0.38	6.27	0.79	10.56	0.28	19.53	0.13
OS		9.97	0.16	17.05	0.32	<u>46.02</u>	<u>0.08</u>	17.30	0.35	4.31	0.90	10.15	0.30	20.06	0.11
FM		11.56	0.06	18.29	0.28	46.93	0.08	23.17	0.19	12.63	0.36	16.64	0.13	29.10	0.04
GC		11.51	0.04	<u>15.96</u>	<u>0.41</u>	47.11	0.09	28.51	0.16	<u>9.43</u>	<u>0.61</u>	19.08	0.06	<u>24.47</u>	<u>0.05</u>
OS		<u>10.82</u>	<u>0.07</u>	<u>16.47</u>	<u>0.42</u>	<u>46.52</u>	<u>0.10</u>	25.63	0.18	<u>9.89</u>	<u>0.53</u>	19.58	0.10	<u>25.75</u>	<u>0.07</u>

The term “BS” stands as the baseline result for images sized 72×72 pixels without occlusion, the bold represents the result of visual occlusion, while the underline marks enhancements in both metrics compared to the bold. “SG” indicates the presence of sunglasses, while “FM” signifies the presence of facemask. “OS” refers to the original skin region method, while “GC” represents GAN-OS with the color transfer method.

On the other hand, ContrastPhys showcases a decreasing trend in results corresponding to the frame rate, especially on its pre-trained dataset UBFC-rPPG, where it shows a clear decreasing trend. This behavior suggests that ContrastPhys relies heavily on power spectrum densities of rPPG signals, and with too few samples, this method does not perform well.

Additionally, results from random frame dropping experiments are summarized in Tables 10–11 across with both mitigation strategies.

DLM generally handle datasets with missing frames more effectively than NLM across most datasets. However, after implementing mitigation strategies, NLM exhibit significant improvements, even outperforming DLM in several datasets.

Furthermore, it is evident that the second mitigation strategy, involving signal reconstruction through linear interpolation, yields superior results compared to the first strategy of recalculating a new FPS. Nonetheless, it is important to note that in scenarios where information loss is substantial, and there is not sufficient data for the second strategy, the results from the first strategy still show considerable improvement compared to having no mitigation strategy at all.

6.4. Artifact influence on face extraction

In real-world settings, extracting faces from frames with artifacts is challenging, often leading to missed extractions. This research introduces artifacts after face extraction to minimize instability caused by missed faces. Although the focus is on how artifacts affect HR estimation, an additional experiment is conducted to explore their impact on face extraction. Using the LGI-PPGI dataset, real-world artifact scenarios are visually simulated to assess face extraction tools such as MediaPipe. These insights contribute to understanding challenges in face extraction amid artifacts.

As observed in the yellow bars “failed_subjects” in Fig. 12, most of the artifacts and color bit reductions introduced in this research did not significantly impact face extraction in subjects, except in three simulated scenarios: adding facemask and sunglasses ranked first, RGB 2 bits second, and adding facemask to the face ranked last. Among these scenarios, the most impactful was the addition of facemask and sunglasses, which failed in extracting faces for 21 out of 26 subjects, although not all frames in failed subjects experienced extraction failure.

Table 9
HR errors: Sample rate variations.

F_s	rPPG Meth.	Dataset															
		COHFACE		LGI-PPGI		MAHNOB		PURE		UBFC-rPPG		UCLA-rPPG		UBFC-Phys			
		MAE	PCC	MAE	PCC	MAE	PCC	MAE	PCC	MAE	PCC	MAE	PCC	MAE	PCC		
NLM																	
BS	OMIT	11.24	0.27	8.79	0.73	36.93	0.02	1.43	0.98	3.49	0.94	3.65	0.56	13.30	0.27		
20				11.99	0.58	37.34	0.01	1.65	0.95	4.10	0.89	4.12	0.55	13.05	0.27		
15				12.57	0.21	11.87	0.63	37.36	0.02	1.22	0.98	3.48	0.94	4.07	0.54	13.13	0.27
10				13.26	0.24	11.50	0.64	37.83	0.00	1.26	0.98	3.35	0.95	4.40	0.49	13.17	0.27
BS	CHROM	12.39	0.21	10.87	0.60	37.13	−0.02	1.42	0.98	3.05	0.97	3.76	0.59	13.65	0.25		
20				12.19	0.57	37.50	−0.01	1.67	0.95	3.81	0.91	4.22	0.56	13.31	0.26		
15				13.93	0.13	13.24	0.59	37.62	0.00	1.24	0.98	3.12	0.96	4.16	0.57	13.40	0.26
10				13.96	0.21	12.87	0.57	38.37	−0.01	1.18	0.99	3.05	0.97	4.95	0.48	13.46	0.25
BS	POS	11.58	0.27	6.05	0.84	36.55	0.03	1.25	0.99	2.74	0.99	3.06	0.65	13.69	0.25		
20				6.93	0.79	37.63	−0.01	1.39	0.98	3.08	0.96	4.02	0.54	13.31	0.26		
15				13.38	0.20	7.85	0.76	37.40	0.02	1.12	0.99	2.79	0.98	4.01	0.53	13.43	0.25
10				14.65	0.23	7.53	0.76	38.42	−0.01	1.29	0.98	2.69	0.99	4.46	0.48	13.57	0.26
DLM																	
BS	EfficientPhys	17.46	0.06	18.33	0.37	38.35	−0.03	10.12	0.50	7.73	0.69	7.99	0.37	15.93	0.17		
20				18.11	0.40	37.43	−0.01	9.62	0.45	9.33	0.59	6.16	0.48	15.07	0.18		
15				15.29	0.07	17.03	0.41	36.85	−0.03	8.81	0.49	6.55	0.74	4.97	0.59	14.51	0.20
10				11.93	0.15	20.13	0.25	36.82	0.05	9.42	0.39	13.27	0.38	5.62	0.52	14.74	0.16
BS	ContrastPhys	9.67	0.22	13.86	0.50	46.52	0.06	11.63	0.59	3.72	0.94	7.13	0.40	16.87	0.17		
20				17.72	0.24	34.92	0.06	8.46	0.49	21.55	−0.11	5.78	0.50	13.68	0.17		
15				15.21	−0.02	24.50	−0.05	45.43	0.01	10.30	0.20	38.45	−0.35	12.94	−0.09	22.86	−0.12
10				23.03	−0.04	33.37	−0.09	52.95	0.03	20.26	−0.05	48.38	−0.17	25.03	−0.11	31.01	−0.01

The bold denotes the baseline result (BS) for images sized 72×72 pixels with the original sample rate while the underlined mark unexpectedly improves in both metrics compared to the BS.

Table 10
HR errors: Missing randomized samples pt. 1.

Lost (%)	rPPG Meth.	Dataset																	
		COHFACE								LGI-PPGI				MAHNOB					
		Strategy 0		Strategy 1		Strategy 2		Strategy 0		Strategy 1		Strategy 2		Strategy 0		Strategy 1		Strategy 2	
		MAE	PCC	MAE	PCC	MAE	PCC	MAE	PCC	MAE	PCC	MAE	PCC	MAE	PCC	MAE	PCC	MAE	PCC
NLM																			
0	OMIT	11.24	0.27					8.79	0.97					36.93	0.02				
10		13.45	0.19	12.64	0.25	11.52	0.26	14.69	0.67	10.02	0.70	9.52	0.69	36.94	0.02	37.02	0.03	36.58	0.04
20		16.87	0.05	13.49	0.22	11.75	0.26	21.93	0.58	12.21	0.63	9.61	0.69	37.16	0.00	37.39	0.01	36.74	0.03
50		24.33	−0.04	26.69	0.13	12.18	0.25	46.72	0.00	16.36	0.61	11.54	0.63	38.63	−0.02	38.10	0.00	36.61	0.05
0	CHRO	12.39	0.21					10.87	0.60					37.13	−0.02				
10		14.92	0.11	13.47	0.19	12.87	0.21	16.51	0.57	11.83	0.60	11.10	0.59	36.65	0.02	37.18	0.00	37.08	−0.02
20		18.02	0.00	14.77	0.16	13.16	0.21	22.82	0.51	13.78	0.55	11.49	0.58	37.26	−0.01	37.71	−0.01	37.01	−0.01
50		22.91	−0.02	30.99	0.11	13.19	0.18	45.95	0.00	17.58	0.57	12.78	0.55	39.18	−0.03	38.54	0.00	36.93	0.00
0	POS	11.58	0.27					6.05	0.84					36.55	0.03				
10		13.59	0.23	12.95	0.25	11.88	0.27	12.44	0.82	7.45	0.80	6.64	0.81	36.69	0.02	37.01	0.01	36.43	0.04
20		17.28	0.13	14.04	0.22	12.01	0.27	20.99	0.76	9.37	0.74	6.76	0.81	36.66	−0.02	37.25	0.01	36.46	0.05
50		27.03	−0.03	27.61	0.12	12.33	0.25	49.26	−0.05	15.74	0.56	7.86	0.76	37.82	0.01	38.50	−0.01	36.65	0.04
DLM																			
0	EP	17.46	0.06					18.33	0.37					38.35	−0.03				
10		17.72	0.06	16.35	0.08	15.19	0.07	19.89	0.38	18.09	0.43	17.71	0.43	38.49	−0.03	38.48	−0.06	38.09	−0.03
20		19.84	0.03	15.61	0.11	13.97	0.10	21.49	0.38	17.49	0.47	16.69	0.46	38.19	−0.02	37.36	0.03	37.08	0.04
50		25.69	0.01	13.65	0.07	12.71	0.12	36.31	−0.11	21.37	0.30	20.91	0.25	38.20	0.01	36.97	0.01	37.98	0.06
0	CP	9.67	0.22					13.86	0.50					46.52	0.06				
10		10.76	0.09	11.62	0.15	11.03	0.14	17.65	0.33	16.83	0.36	16.10	0.36	46.00	0.08	43.64	0.07	43.14	0.08
20		13.14	−0.10	14.33	0.03	13.44	0.03	21.14	0.18	18.76	0.30	18.27	0.21	46.42	0.07	41.42	0.06	41.15	0.05
50		12.25	0.01	30.62	0.06	18.86	0.02	29.28	−0.41	30.48	0.02	27.12	0.00	43.53	0.10	41.75	0.06	39.57	0.08

The bold denotes the baseline result (BS) for images sized 72×72 pixels with 0% lost sample.

Further analysis focuses on the number of frames that failed to be extracted in specific subjects, as shown in the blue bar in Fig. 12. Notably, adding blur to datasets did not significantly affect MediaPipe face extraction, and in some cases, it even improved detection, as seen in the “alex_talk” subject. Surprisingly, reducing the original RGB 8 bits to 6 bits yielded a similar improvement in the “felix_rotation” subject. A trend in failed face extraction across transformation types is observed, with occurrences being most common in subjects “alex”, “cpi”, and

“felix”, particularly during specific tasks such as talking, rotation, and gym activities.

Although face extraction failures were not as pronounced as one might expect, certain scenarios, like “angelo_gym” and “cpi_talk”, exhibited face extraction failures exceeding 50%, which could significantly impact HR estimation. Mitigation strategies, such as using previously (or later) detected landmarks to extract faces or employing random missing frames mitigation strategies as those proposed before,

Table 11
HR errors: Missing randomized samples pt. 2.

Lost(%)	rPPG Meth.	Dataset											
		PURE						UBFC-rPPG					
		Strategy 0		Strategy 1		Strategy 2		Strategy 0		Strategy 1		Strategy 2	
		MAE	PCC	MAE	PCC	MAE	PCC	MAE	PCC	MAE	PCC	MAE	PCC
NLM													
0	OMIT	1.43	0.98					3.49	0.94				
10		7.32	0.96	2.59	0.97	1.46	0.97	8.80	0.90	5.38	0.94	3.46	0.94
20		16.57	0.93	3.18	0.96	1.43	0.97	20.92	0.82	6.32	0.93	3.48	0.94
50		55.57	0.31	7.45	0.85	1.69	0.96	62.75	0.15	12.83	0.76	3.65	0.94
0	CHROM	1.42	0.98					3.05	0.97				
10		7.43	0.95	2.61	0.97	1.40	0.98	8.37	0.94	4.96	0.96	3.06	0.97
20		16.61	0.93	3.27	0.96	1.48	0.97	20.66	0.87	6.04	0.94	3.18	0.96
50		55.93	0.37	7.17	0.87	1.63	0.96	62.34	0.06	13.54	0.65	3.29	0.96
0	POS	1.25	0.99					2.74	0.99				
10		7.22	0.98	2.45	0.98	1.26	0.99	8.16	0.96	4.78	0.97	2.78	0.98
20		16.78	0.94	3.28	0.96	1.23	0.99	20.27	0.92	5.95	0.95	2.80	0.98
50		56.02	0.31	8.53	0.74	1.64	0.97	65.89	0.20	12.19	0.78	3.03	0.97
DLM													
0	EfficientPhys	10.12	0.50					7.73	0.69				
10		14.72	0.32	12.23	0.33	10.31	0.45	13.86	0.57	9.90	0.68	7.71	0.71
20		19.45	0.32	11.01	0.47	9.06	0.54	24.00	0.43	11.69	0.62	8.58	0.65
50		40.61	−0.10	14.27	0.32	10.93	0.30	44.26	−0.17	19.49	0.45	14.46	0.43
0	ContrastPhys	11.63	0.59					3.72	0.94				
10		11.97	0.74	10.67	0.58	9.39	0.61	8.24	0.91	6.29	0.91	3.96	0.94
20		18.26	0.66	10.04	0.52	7.65	0.58	17.82	0.62	11.93	0.64	7.57	0.71
50		45.80	−0.10	14.47	0.22	10.44	0.25	23.93	−0.21	39.64	−0.01	36.47	−0.14
Lost (%)	rPPG Meth.	Dataset											
		UCLA-rPPG						UBFC-Phys					
		Strategy 0		Strategy 1		Strategy 2		Strategy 0		Strategy 1		Strategy 2	
		MAE	PCC	MAE	PCC	MAE	PCC	MAE	PCC	MAE	PCC	MAE	PCC
NLM													
0	OMIT	3.65	0.56					13.30	0.27				
10		10.47	0.60	4.87	0.55	3.45	0.60	18.90	0.25	13.28	0.27	13.30	0.27
20		19.59	0.56	5.69	0.51	3.55	0.59	27.22	0.24	13.56	0.27	13.29	0.27
50		58.04	0.21	9.70	0.41	3.38	0.66	56.45	0.07	15.01	0.21	13.11	0.28
0	CHROM	3.76	0.59					13.65	0.25				
10		10.76	0.59	4.93	0.58	3.72	0.60	19.17	0.24	13.72	0.24	13.62	0.25
20		19.82	0.53	5.84	0.52	3.83	0.59	27.11	0.24	13.61	0.26	13.56	0.25
50		57.28	0.14	10.14	0.41	3.79	0.61	55.41	0.07	14.70	0.23	13.38	0.26
0	POS	3.06	0.65					13.69	0.25				
10		10.26	0.65	4.47	0.59	3.24	0.63	19.59	0.23	13.70	0.24	13.67	0.25
20		19.79	0.60	5.59	0.52	3.33	0.61	28.20	0.23	13.64	0.25	13.62	0.25
50		60.19	0.32	9.32	0.45	3.36	0.64	59.58	0.09	14.89	0.22	13.47	0.26
DLM													
0	EfficientPhys	7.99	0.37					15.93	0.17				
10		12.45	0.38	7.78	0.41	7.40	0.38	19.42	0.18	16.34	0.16	15.77	0.17
20		19.80	0.29	8.71	0.36	6.75	0.45	24.50	0.13	16.25	0.16	15.50	0.19
50		39.79	0.00	11.16	0.33	6.41	0.47	37.64	0.00	17.32	0.12	15.31	0.17
0	ContrastPhys	7.13	0.40					16.87	0.17				
10		12.66	0.54	6.22	0.52	5.20	0.55	21.61	0.24	14.44	0.23	14.21	0.25
20		20.00	0.61	5.73	0.61	4.29	0.65	28.42	0.30	12.79	0.30	12.56	0.31
50		37.13	−0.14	15.95	0.02	11.89	0.03	40.92	−0.01	19.11	0.03	17.55	0.04

The bold denotes the baseline result (BS) for images sized 72×72 pixels with 0% lost sample.

can help mitigate the impact of failed extractions. However, it is important to note that these strategies are only effective if accurate face detection is possible.

7. Conclusion

This article highlights that rPPG extraction in real-world conditions is affected by complex challenges due to artifacts such as spatial, temporal, and visual occlusions, which require an extensive evaluation approach. Through realistic simulation and comparative experimentation, detailed insights into the effects of these factors on the performance of HR estimation from video streams were observed.

Regarding face extraction under artifacts, the findings indicate that most introduced artifacts and color bit reductions had negligible effects on face extraction in subjects. However, the addition of facemask and sunglasses proved more challenging which led to extraction failures in a limited number of datasets. Although face extraction failures were not as bad as maybe expected, the analysis underscores the importance of employing mitigation strategies such as utilizing previously detected landmarks or careful timestamping of the frames to reconstruct signals with a significant amount of randomly missing samples.

The resolution of the facial regions was found to have minimal impact on HR estimation, with certain methods even showing slight improvements at specific sizes, maybe due to the low-pass filtering

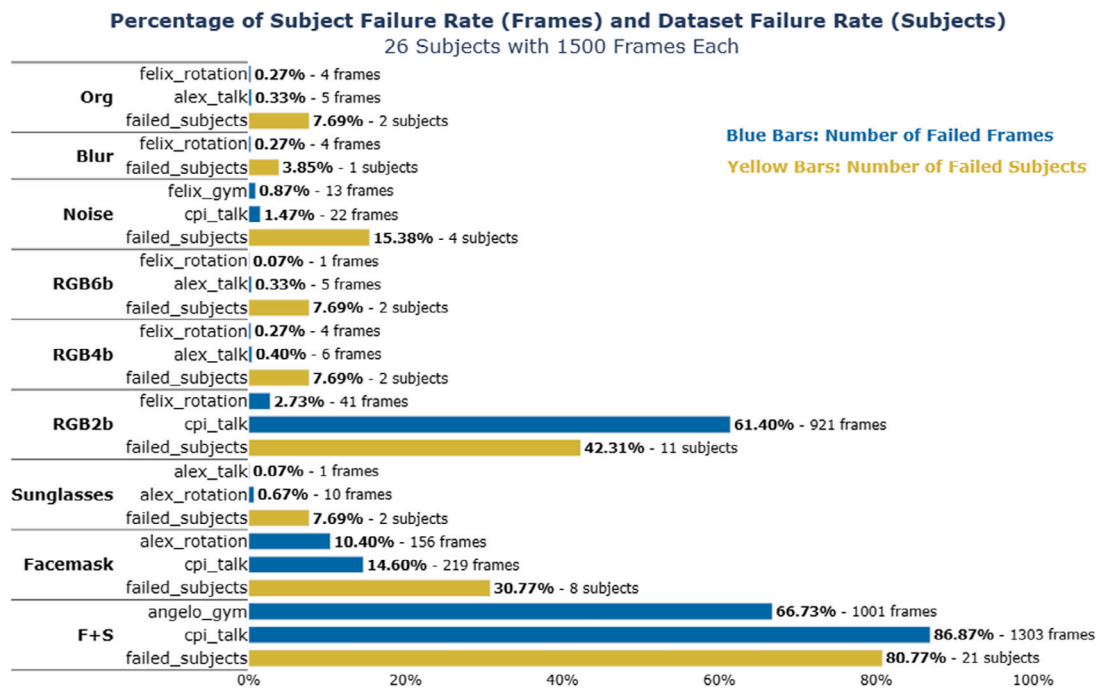


Fig. 12. Artifact influence on LGI-PPGI dataset.

effects caused by the downsizing of the regions. Notably, the choice of input size for comparison emerged as a crucial consideration, especially when dealing with DLM that require very specific input formats.

The reduction in bit depth consistently influenced HR estimation performance, with lower bit depths leading to lower performance, especially for heavy reductions. On the other hand, the impact of image degradation effects such as blur and noise varied across datasets and methods. Among those blur had a mild effect and occasionally even improved performance, maybe also due to the spurious low pass filtering effect caused by averaging neighboring pixels. Comparatively, noise consistently exerted a more pronounced adverse effect, particularly on NLM. Although denoising techniques showed promise in improving image quality, their corresponding impact on HR estimation performance was not significant.

Visual occlusions posed challenges to HR estimation accuracy, with facemask significantly impairing performance while sunglasses had minimal impact. Mitigation strategies varied in effectiveness. DLM showed considerable improvements in the facemask scenario, but the performance of a simple inpainting method such as removing the occluded skin regions showed better results in HR estimation, while more sophisticated inpainting methods such as GAN-based had superior performance in face visualization that did not translate to heart-rate estimation.

Furthermore, the analysis of frame rate variations revealed intriguing behavior in DLM, with EfficientPhys demonstrating improved performance at lower frame rates in most datasets, except for UBFC-rPPG. ContrastPhys, a method that worked relatively well in all types of datasets due to its unsupervised nature, presented specific challenges at lower frame rates. On the other hand, the results for NLM remained relatively consistent with minor fluctuations across datasets. In the context of random sample missing scenarios, the experiment showed the comparative performance of NLM and DLM, with DLM generally handling missing frames more effectively. However, mitigation strategies significantly improved the performance of NLM, sometimes even beyond DLM, particularly through signal reconstruction using careful timestamping, which underscores the importance of being aware of potential data loss effects. These proposed mitigation strategies could extend to other physiological measurement modalities, such as

electroencephalography or electrocardiography, which increasingly operate as wireless wearable devices, benefiting applications like epilepsy seizure detection [84] and emotion monitoring [85].

In conclusion, this paper significantly advances rPPG research, particularly in challenging scenarios, a relatively underexplored area. A comparison with prior studies shows notable improvements in key aspects. While Yue et al. [31] focus on developing DL models for low-resolution videos, Speth et al. [28] extend this to face mask videos. Álvarez Casado et al. [14] consider frame resolution variability and networking factors for only NLM. In contrast, Nguyen et al. [16] use both NLM and DLM but only concentrate solely on visual occlusion and spatial factors. This paper integrates spatial information, temporal factors, and visual occlusion, introducing strategies to mitigate data degradation before rPPG calculation. These advancements demonstrate the potential for improved accuracy across all rPPG methods rather than specific ones, this generalizability is crucial for practical applications, where diverse scenarios and data quality variations exist. Furthermore, this work advances the understanding of rPPG methodologies and provides practical insights for improving real-world performance. Future research could concentrate on improving mitigation strategies and investigating additional factors that influence rPPG performance in various scenarios.

CRediT authorship contribution statement

Nhi Nguyen: Writing – review & editing, Writing – original draft, Visualization, Validation, Software, Methodology, Investigation, Formal analysis, Conceptualization. **Le Nguyen:** Writing – review & editing, Writing – original draft, Supervision, Methodology, Investigation, Formal analysis, Conceptualization. **Honghan Li:** Writing – original draft, Visualization, Software, Methodology. **Miguel Bordallo López:** Writing – review & editing, Writing – original draft, Methodology, Investigation, Funding acquisition, Conceptualization. **Constantino Álvarez Casado:** Writing – review & editing, Writing – original draft, Visualization, Validation, Supervision, Software, Methodology, Investigation, Formal analysis, Conceptualization.

Declaration of competing interest

The authors declare that they have no known competing financial interests or personal relationships that could have appeared to influence the work reported in this paper.

Acknowledgments

The authors would like to express their sincere appreciation to the funding agencies that supported this study. Specific acknowledgment is given to the Academy of Finland 6G Flagship program (Grant 346208) and PROFIS HiDyn (Grant 326291) for their aid. Gratitude is also extended to the Japan Society for the Promotion of Science (JSPS) for their support under KAKENHI Grant number 21J22170 and Infotech Oulu.

Appendix A. Supplementary data

Supplementary material related to this article can be found online at <https://doi.org/10.1016/j.combiomed.2024.108873>.

References

- [1] B. Huang, S. Hu, Z. Liu, C.-L. Lin, J. Su, C. Zhao, L. Wang, W. Wang, Challenges and prospects of visual contactless physiological monitoring in clinical study, *NPJ Digit. Med.* 6 (1) (2023) 231, <http://dx.doi.org/10.1038/s41746-023-00973-x>.
- [2] C. Álvarez Casado, M. Bordallo López, Face2PPG: An unsupervised pipeline for blood volume pulse extraction from faces, *IEEE J. Biomed. Health Inf.* (2023) 1–12, <http://dx.doi.org/10.1109/JBHI.2023.3307942>.
- [3] G. Boccignone, D. Conte, V. Cuculo, A. D'Amelio, G. Grossi, R. Lanzarotti, An open framework for remote-PPG methods and their assessment, *IEEE Access* 8 (2020) 216083–216103, <http://dx.doi.org/10.1109/ACCESS.2020.3040936>.
- [4] C. Stickel, M. Ebner, S. Steinbach-Nordmann, G. Searle, A. Holzinger, Emotion detection: application of the valence arousal space for rapid biological usability testing to enhance universal access, in: *Universal Access in Human-Computer Interaction. Addressing Diversity: 5th International Conference, UAHCI 2009, Held As Part of HCI International 2009, San Diego, CA, USA, July 19–24, 2009. Proceedings, Part I* 5, Springer, 2009, pp. 615–624, http://dx.doi.org/10.1007/978-3-642-02707-9_70.
- [5] R. Cittadini, C. Tamantini, F. Scotto di Luzio, C. Lauretti, L. Zollo, F. Cordella, Affective state estimation based on Russell's model and physiological measurements, *Sci. Rep.* 13 (1) (2023) 9786, <http://dx.doi.org/10.1038/s41598-023-36915-6>.
- [6] Y. Du, R.G. Crespo, O.S. Martínez, Human emotion recognition for enhanced performance evaluation in e-learning, *Prog. Artif. Intell.* 12 (2) (2023) 199–211, <http://dx.doi.org/10.1007/s13748-022-00278-2>.
- [7] C. Álvarez Casado, P. Paananen, P. Siirtola, S. Pirttikangas, M. Bordallo López, Meditation detection using sensors from wearable devices, in: *Adjunct Proceedings of the 2021 ACM International Joint Conference on Pervasive and Ubiquitous Computing and Proceedings of the 2021 ACM International Symposium on Wearable Computers*, 2021, pp. 112–116, <http://dx.doi.org/10.1145/3460418.3479318>.
- [8] C. Álvarez Casado, P. Räsänen, L.N. Nguyen, A. Lämsä, J. Peltola, M. Bordallo López, A distributed framework for remote multimodal biosignal acquisition and analysis, in: *Nordic Conference on Digital Health and Wireless Solutions*, Springer, 2024, pp. 127–146, http://dx.doi.org/10.1007/978-3-031-59091-7_9.
- [9] M. Debevc, P. Kosec, A. Holzinger, Improving multimodal web accessibility for deaf people: sign language interpreter module, *Multimedia Tools Appl.* 54 (2011) 181–199, <http://dx.doi.org/10.1007/s11042-010-0529-8>.
- [10] A. Caduff, Y. Feldman, P.B. Ishaq, S. Launer, Physiological monitoring and hearing loss: toward a more integrated and ecologically validated health mapping, *Ear Hear.* 41 (2020) 120S–130S, <http://dx.doi.org/10.1097/AUD.0000000000000960>.
- [11] T. Curran, D. McDuff, X. Liu, G. Narayanswamy, C. Ma, S. Patel, E. Yang, Camera-based remote photoplethysmography for blood pressure measurement: current evidence, clinical perspectives, and future applications, *Connect. Health Telemed.* 2 (2023) 200004, <http://dx.doi.org/10.20517/chatmed.2022.025>.
- [12] M. Rapczynski, P. Werner, A. Al-Hamadi, Effects of video encoding on camera based heart rate estimation, *IEEE Trans. Biomed. Eng.* PP (2019) 1, <http://dx.doi.org/10.1109/TBME.2019.2904326>.
- [13] J. Williams, J. Francombe, D. Murphy, Evaluating the influence of room illumination on camera-based physiological measurements for the assessment of screen-based media, *Appl. Sci.* 13 (2023) 8482, <http://dx.doi.org/10.3390/app13148482>.
- [14] C. Álvarez Casado, L. Nguyen, O. Silvén, M. Bordallo López, Assessing the feasibility of remote photoplethysmography through videocalls: A study of network and computing constraints, in: *Scandinavian Conference on Image Analysis*, Springer, 2023, pp. 586–598, http://dx.doi.org/10.1007/978-3-031-31438-4_38.
- [15] D.J. McDuff, E.B. Blackford, J.R. Estepp, The impact of video compression on remote cardiac pulse measurement using imaging photoplethysmography, in: *2017 12th IEEE International Conference on Automatic Face & Gesture Recognition, FG 2017*, 2017, pp. 63–70, <http://dx.doi.org/10.1109/FG.2017.17>.
- [16] N. Nguyen, L.N. Nguyen, C. Álvarez Casado, O. Silvén, M. Bordallo López, Non-contact heart rate measurement from deteriorated videos, in: *2023 IEEE 28th International Conference on Emerging Technologies and Factory Automation, ETFA, 2023*, pp. 1–8, <http://dx.doi.org/10.1109/ETFA54631.2023.10275673>.
- [17] G. Heusch, A. Anjos, S. Marcel, A reproducible study on remote heart rate measurement, 2017, *CoRR* abs/1709.00962, [arXiv:1709.00962](http://arxiv.org/abs/1709.00962).
- [18] C.S. Pilz, S. Zaunseder, J. Krajewski, V. Blazek, Local group invariance for heart rate estimation from face videos in the wild, in: *2018 IEEE/CVF Conference on Computer Vision and Pattern Recognition Workshops, CVPRW, 2018*, pp. 1335–13358, <http://dx.doi.org/10.1109/CVPRW.2018.00172>.
- [19] M. Soleymani, J. Lichtenauer, T. Pun, M. Pantic, A multimodal database for affect recognition and implicit tagging, *IEEE Trans. Affect. Comput.* 3 (1) (2012) 42–55, <http://dx.doi.org/10.1109/T-AFFC.2011.25>.
- [20] R. Stricker, S. Müller, H.-M. Gross, Non-contact video-based pulse rate measurement on a mobile service robot, in: *The 23rd IEEE International Symposium on Robot and Human Interactive Communication*, 2014, pp. 1056–1062, <http://dx.doi.org/10.1109/ROMAN.2014.6926392>.
- [21] S. Bobbia, R. Macwan, Y. Benezeth, A. Mansouri, J. Dubois, Unsupervised skin tissue segmentation for remote photoplethysmography, *Pattern Recognit. Lett.* 124 (2019) 82–90, <http://dx.doi.org/10.1016/j.patrec.2017.10.017>.
- [22] Z. Wang, Y. Ba, P. Chari, O.D. Bozkurt, G. Brown, P. Patwa, N. Vaddi, L. Jalilian, A. Kadambi, Synthetic generation of face videos with plethysmograph physiology, in: *2022 IEEE/CVF Conference on Computer Vision and Pattern Recognition, CVPR, 2022*, pp. 20555–20564, <http://dx.doi.org/10.1109/CVPR52688.2022.01993>.
- [23] R.M. Sabour, Y. Benezeth, P. De Oliveira, J. Chappé, F. Yang, UBFC-Phys: A multimodal database for psychophysiological studies of social stress, *IEEE Trans. Affect. Comput.* 14 (1) (2023) 622–636, <http://dx.doi.org/10.1109/TAFFC.2021.3056960>.
- [24] Y. Sun, N. Thakor, Photoplethysmography revisited: From contact to noncontact, from point to imaging, *IEEE Trans. Biomed. Eng.* 63 (3) (2016) 463–477, <http://dx.doi.org/10.1109/TBME.2015.2476337>.
- [25] R. Song, S. Zhang, J. Cheng, C. Li, X. Chen, New insights on super-high resolution for video-based heart rate estimation with a semi-blind source separation method, *Comput. Biol. Med.* 116 (2020) 103535, <http://dx.doi.org/10.1016/j.combiomed.2019.103535>.
- [26] K. Setchfield, A. Gorman, A.H.R. Simpson, M.G. Somekh, A.J. Wright, Effect of skin color on optical properties and the implications for medical optical technologies: a review, *J. Biomed. Opt.* 29 (1) (2024) 010901, <http://dx.doi.org/10.1117/1.JBO.29.1.010901>.
- [27] Y.-C. Lin, Y.-H. Lin, A study of color illumination effect on the SNR of rPPG signals, in: *2017 39th Annual International Conference of the IEEE Engineering in Medicine and Biology Society, EMBC, 2017*, pp. 4301–4304, <http://dx.doi.org/10.1109/EMBC.2017.8037807>.
- [28] J. Speth, N. Vance, P. Flynn, K. Bowyer, A. Czajka, Remote pulse estimation in the presence of face masks, in: *IEEE/CVF Conference on Computer Vision and Pattern Recognition Workshops, 2022*, pp. 2085–2094, <http://dx.doi.org/10.1109/CVPRW56347.2022.00226>.
- [29] Y. Mironenko, K. Kalinin, M. Kopeliovich, M. Petrushan, Remote photoplethysmography: Rarely considered factors, in: *2020 IEEE/CVF Conference on Computer Vision and Pattern Recognition Workshops, CVPRW, 2020*, pp. 1197–1206, <http://dx.doi.org/10.1109/CVPRW50498.2020.00156>.
- [30] Z. Yu, W. Peng, X. Li, X. Hong, G. Zhao, Remote heart rate measurement from highly compressed facial videos: An end-to-end deep learning solution with video enhancement, in: *IEEE/CVF International Conference on Computer Vision, ICCV, 2019*, pp. 151–160, <http://dx.doi.org/10.1109/ICCV.2019.00024>.
- [31] Z. Yue, S. Ding, S. Yang, H. Yang, Z. Li, Y. Zhang, Y. Li, Deep super-resolution network for rPPG information recovery and noncontact heart rate estimation, *IEEE Trans. Instrum. Meas.* (2021) 1–11, <http://dx.doi.org/10.1109/TIM.2021.3109398>.
- [32] F. Haugg, M. Elgendi, C. Menon, Effectiveness of remote PPG construction methods: A preliminary analysis, *Bioengineering* 9 (10) (2022) <http://dx.doi.org/10.3390/bioengineering9100485>.
- [33] W. Verkruysse, L.O. Svaasand, J.S. Nelson, Remote plethysmographic imaging using ambient light, *Opt. Express* 16 (26) (2008) 21434–21445, <http://dx.doi.org/10.1364/OE.16.021434>.
- [34] R. Castellano Ontiveros, M. Elgendi, G. Missale, C. Menon, Evaluating RGB channels in remote photoplethysmography: a comparative study with contact-based PPG, *Front. Physiol.* 14 (2023) 1296277, <http://dx.doi.org/10.3389/fphys.2023.1296277>.
- [35] M. Kumar, J. Suliburk, A. Veeraraghavan, A. Sabharwal, PulseCam: a camera-based, motion-robust and highly sensitive blood perfusion imaging modality, *Sci. Rep.* 10 (1) (2020) 4825, <http://dx.doi.org/10.1038/s41598-020-61576-0>.

- [36] G. Boccignone, D. Conte, V. Cuculo, A. D'Amelio, G. Grossi, R. Lanzarotti, E. Mortara, pyVHR: a python framework for remote photoplethysmography, *PeerJ Comput. Sci.* 8 (2022) e929, <http://dx.doi.org/10.7717/peerj.cs.929>.
- [37] A.K. Maity, J. Wang, A. Sabharwal, S.K. Nayar, RobustPPG: camera-based robust heart rate estimation using motion cancellation, *Biomed. Opt. Express* 13 (10) (2022) 5447–5467, <http://dx.doi.org/10.1364/BOE.465143>.
- [38] D. Botina-Monsalve, Y. Benezeth, R. Macwan, P. Pierrart, F. Parra, K. Nakamura, R. Gomez, J. Miteran, Long short-term memory deep-filter in remote photoplethysmography, in: 2020 IEEE/CVF Conference on Computer Vision and Pattern Recognition Workshops, CVPRW, 2020, pp. 1242–1249, <http://dx.doi.org/10.1109/CVPRW50498.2020.00161>.
- [39] M. Lewandowska, J. Rumiński, T. Kocejko, J. Nowak, Measuring pulse rate with a webcam — A non-contact method for evaluating cardiac activity, in: Federated Conference on Computer Science and Information Systems, FedCSIS, 2011, pp. 405–410, URL <https://api.semanticscholar.org/CorpusID:1926655>.
- [40] M.-Z. Poh, D.J. McDuff, R.W. Picard, Advancements in noncontact, multiparameter physiological measurements using a webcam, *IEEE Trans. Biomed. Eng.* 58 (1) (2011) 7–11, <http://dx.doi.org/10.1109/TBME.2010.2086456>.
- [41] G. de Haan, V. Jeanne, Robust pulse rate from chrominance-based rPPG, *IEEE Trans. Biomed. Eng.* 60 (10) (2013) 2878–2886, <http://dx.doi.org/10.1109/TBME.2013.2266196>.
- [42] W. Wang, A.C. den Brinker, S. Stuijk, G. de Haan, Algorithmic principles of remote PPG, *IEEE Trans. Biomed. Eng.* 64 (7) (2017) 1479–1491, <http://dx.doi.org/10.1109/TBME.2016.2609282>.
- [43] X. Li, J. Chen, G. Zhao, M. Pietikäinen, Remote heart rate measurement from face videos under realistic situations, in: 2014 IEEE Conference on Computer Vision and Pattern Recognition, 2014, pp. 4264–4271, <http://dx.doi.org/10.1109/CVPR.2014.543>.
- [44] W. Wang, A. den Brinker, G. Haan, Discriminative signatures for remote-PPG, *IEEE Trans. Biomed. Eng. PP* (2019) 1, <http://dx.doi.org/10.1109/TBME.2019.2938564>.
- [45] E.M. Nowara, D. McDuff, A. Veeraraghavan, The benefit of distraction: Denoising camera-based physiological measurements using inverse attention, in: 2021 IEEE/CVF International Conference on Computer Vision, ICCV, 2021, pp. 4935–4944, <http://dx.doi.org/10.1109/ICCV48922.2021.00491>.
- [46] M. Kumar, A. Veeraraghavan, A. Sabharwal, Distanceppg: Robust non-contact vital signs monitoring using a camera, *Biomed. Opt. Express* 6 (5) (2015) 1565–1588, <http://dx.doi.org/10.1364/BOE.6.001565>.
- [47] F. Haugg, M. Elgendi, C. Menon, GRGB rPPG: An efficient low-complexity remote photoplethysmography-based algorithm for heart rate estimation, *Bioengineering* 10 (2) (2023) <http://dx.doi.org/10.3390/bioengineering10020243>.
- [48] R. Špetlík, V. Franc, J. Matas, Visual heart rate estimation with convolutional neural network, in: Proceedings of the British Machine Vision Conference, Newcastle, UK, 2018, pp. 3–6, URL <https://api.semanticscholar.org/CorpusID:52219725>.
- [49] W. Chen, D. McDuff, DeepPhys: Video-based physiological measurement using convolutional attention networks, in: Computer Vision – ECCV 2018: 15th European Conference, Munich, Germany, September 8–14, 2018, Proceedings, Part II, Springer-Verlag, Berlin, Heidelberg, 2018, pp. 356–373, http://dx.doi.org/10.1007/978-3-030-01216-8_22.
- [50] X. Niu, S. Shan, H. Han, X. Chen, Rhythmnet: End-to-end heart rate estimation from face via spatial-temporal representation, *IEEE Trans. Image Process.* 29 (2019) 2409–2423, <http://dx.doi.org/10.1109/TIP.2019.2947204>.
- [51] Z. Yu, X. Li, X. Niu, J. Shi, G. Zhao, Autohr: A strong end-to-end baseline for remote heart rate measurement with neural searching, *IEEE Signal Process. Lett.* 27 (2020) 1245–1249, <http://dx.doi.org/10.1109/LSP.2020.3007086>.
- [52] E. Lee, E. Chen, C.-Y. Lee, Meta-rPPG: Remote heart rate estimation using a transductive meta-learner, in: A. Vedaldi, H. Bischof, T. Brox, J.-M. Frahm (Eds.), *Computer Vision – ECCV 2020*, Springer International Publishing, Cham, 2020, pp. 392–409, http://dx.doi.org/10.1007/978-3-030-58583-9_24.
- [53] R. Song, H. Chen, J. Cheng, C. Li, Y. Liu, X. Chen, PulseGAN: Learning to generate realistic pulse waveforms in remote photoplethysmography, *IEEE J. Biomed. Health Inf. PP* (2021) 1, <http://dx.doi.org/10.1109/JBHI.2021.3051176>.
- [54] B. Lokendra, G. Puneet, AND-rPPG: A novel denoising-rPPG network for improving remote heart rate estimation, *Comput. Biol. Med.* 141 (2022) 105146, <http://dx.doi.org/10.1016/j.combiomed.2021.105146>.
- [55] X. Liu, J. Fromm, S. Patel, D. McDuff, Multi-task temporal shift attention networks for on-device contactless vitals measurement, in: Proceedings of the 34th International Conference on Neural Information Processing Systems, NIPS '20, Curran Associates Inc., Red Hook, NY, USA, 2020, URL <https://api.semanticscholar.org/CorpusID:219530885>.
- [56] Z. Yu, Y. Shen, J. Shi, H. Zhao, P. Torr, G. Zhao, PhysFormer: Facial video-based physiological measurement with temporal difference transformer, in: 2022 IEEE/CVF Conference on Computer Vision and Pattern Recognition, CVPR, IEEE Computer Society, Los Alamitos, CA, USA, 2022, pp. 4176–4186, <http://dx.doi.org/10.1109/CVPR52688.2022.00415>.
- [57] X. Liu, B. Hill, Z. Jiang, S. Patel, D. McDuff, EfficientPhys: Enabling simple, fast and accurate camera-based cardiac measurement, in: Proceedings of the IEEE/CVF Winter Conference on Applications of Computer Vision, WACV, 2023, pp. 5008–5017, <http://dx.doi.org/10.1109/WACV56688.2023.00498>.
- [58] J. Gideon, S. Stent, The way to my heart is through contrastive learning: Remote photoplethysmography from unlabelled video, in: 2021 IEEE/CVF International Conference on Computer Vision, ICCV, IEEE Computer Society, Los Alamitos, CA, USA, 2021, pp. 3975–3984, <http://dx.doi.org/10.1109/ICCV48922.2021.00396>.
- [59] J. Speth, N. Vance, P. Flynn, A. Czajka, Non-contrastive unsupervised learning of physiological signals from video, in: 2023 IEEE/CVF Conference on Computer Vision and Pattern Recognition, CVPR, IEEE Computer Society, Los Alamitos, CA, USA, 2023, pp. 14464–14474, <http://dx.doi.org/10.1109/CVPR52729.2023.01390>.
- [60] Z. Sun, X. Li, Contrast-phys: Unsupervised video-based remote physiological measurement via spatiotemporal contrast, in: S. Avidan, G. Brostow, M. Cissé, G.M. Farinella, T. Hassner (Eds.), *Computer Vision – ECCV 2022*, Springer Nature Switzerland, Cham, 2022, pp. 492–510, http://dx.doi.org/10.1007/978-3-031-19775-8_29.
- [61] L. Zhang, G. Su, J. Yin, Y. Li, Q. Lin, X. Zhang, L. Shao, Bioinspired scene classification by deep active learning with remote sensing applications, *IEEE Trans. Cybern.* 52 (7) (2021) 5682–5694, <http://dx.doi.org/10.1109/TCYB.2020.2981480>.
- [62] C.-H. Cheng, K.-L. Wong, J.-W. Chin, T.-T. Chan, R.H.Y. So, Deep learning methods for remote heart rate measurement: A review and future research agenda, *Sensors* 21 (18) (2021) <http://dx.doi.org/10.3390/s21186296>.
- [63] Q. Zhan, W. Wang, G. de Haan, Analysis of CNN-based remote-PPG to understand limitations and sensitivities, *Biomed. Opt. Express* 11 (3) (2020) 1268–1283, <http://dx.doi.org/10.1364/BOE.382637>.
- [64] L.-l. Zhao, X.-l. Jiang, L.-m. Li, G.-q. Zeng, H.-j. Liu, Optimization of a robust collaborative-relay beamforming design for simultaneous wireless information and power transfer, *Front. Inf. Technol. Electron. Eng.* 19 (11) (2018) 1432–1443, <http://dx.doi.org/10.1631/FITEE.1601268>.
- [65] S. Hanfland, M. Paul, Video format dependency of PPGI signals, in: Proceedings of the International Conference on Electrical Engineering, Vol. 1, 2016, p. 2, URL https://poster.fel.cvut.cz/poster2016/proceedings/Section_BI/BI_007_Hanfland.pdf.
- [66] C. Zhao, C.-L. Lin, W. Chen, Z. Li, A novel framework for remote photoplethysmography pulse extraction on compressed videos, in: 2018 IEEE/CVF Conference on Computer Vision and Pattern Recognition Workshops, CVPRW, 2018, pp. 1380–138009, <http://dx.doi.org/10.1109/CVPRW.2018.00177>.
- [67] L. Lampier, A. Floriano, D. Delisle Rodriguez, E. Caldeira, T. Bastos-Filho, Effect of image resolution on remote photoplethysmography: Towards emotion detection in children with autism spectrum disorder, in: Annals of the 14th Brazilian Symposium on Intelligent Automation, 2019, pp. 835–849, <http://dx.doi.org/10.17648/sbai-2019-111242>.
- [68] Y. Sun, S. Hu, V. Azorin Peris, R. Kalawsky, S. Greenwald, Noncontact imaging photoplethysmography to effectively access pulse rate variability, *J. Biomed. Opt.* 18 (2013) 61205, <http://dx.doi.org/10.1117/1.JBO.18.6.061205>.
- [69] E.B. Blackford, J.R. Estepp, Effects of frame rate and image resolution on pulse rate measured using multiple camera imaging photoplethysmography, in: B. Gimi, R.C. Molthen (Eds.), *Medical Imaging 2015: Biomedical Applications in Molecular, Structural, and Functional Imaging*, in: Society of Photo-Optical Instrumentation Engineers (SPIE) Conference Series, vol. 9417, 2015, p. 94172D, <http://dx.doi.org/10.1117/12.2083940>.
- [70] C. Zhao, W. Chen, C.-L. Lin, X. Wu, Physiological signal preserving video compression for remote photoplethysmography, *IEEE Sens. J.* 19 (12) (2019) 4537–4548, <http://dx.doi.org/10.1109/JSEN.2019.2899102>.
- [71] D. Botina-Monsalve, Y. Benezeth, J. Miteran, Rtrppg: An ultra light 3DCNN for real-time remote photoplethysmography, in: 2022 IEEE/CVF Conference on Computer Vision and Pattern Recognition Workshops, CVPRW, 2022, pp. 2145–2153, <http://dx.doi.org/10.1109/CVPRW56347.2022.00233>.
- [72] C. Lugesesi, J. Tang, H. Nash, C. McClanahan, E. Uboweja, M. Hays, F. Zhang, C.-L. Chang, M. Yong, J. Lee, W.-T. Chang, W. Hua, M. Georg, M. Grundmann, MediaPipe: A framework for perceiving and processing reality, in: Third Workshop on Computer Vision for AR/VR At IEEE Computer Vision and Pattern Recognition (CVPR) 2019, 2019, URL <https://api.semanticscholar.org/CorpusID:211545181>.
- [73] V. Bazarevsky, Y. Kartynnik, A. Vakunov, K. Raveendran, M. Grundmann, BlazeFace: Sub-millisecond neural face detection on mobile GPUs, 2019, CoRR [arXiv:1907.05047](https://arxiv.org/abs/1907.05047).
- [74] Y. Kartynnik, A. Ablavatski, I. Grishchenko, M. Grundmann, Real-time facial surface geometry from monocular video on mobile GPUs, 2019, CoRR [arXiv:1907.06724](https://arxiv.org/abs/1907.06724).
- [75] X. Niu, H. Han, S. Shan, X. Chen, VIPL-HR: A multi-modal database for pulse estimation from less-constrained face video, in: C. Jawahar, H. Li, G. Mori, K. Schindler (Eds.), *Computer Vision – ACCV 2018*, Springer International Publishing, Cham, 2019, pp. 562–576, http://dx.doi.org/10.1007/978-3-030-20873-8_36.
- [76] J.R. Estepp, E.B. Blackford, C.M. Meier, Recovering pulse rate during motion artifact with a multi-imager array for non-contact imaging photoplethysmography, in: 2014 IEEE International Conference on Systems, Man, and Cybernetics, SMC, 2014, pp. 1462–1469, <http://dx.doi.org/10.1109/SMC.2014.6974121>.
- [77] G. Bradski, The OpenCV library, Dr. Dobb's J. Softw. Tools (2000) URL <http://opencv.org/>.

- [78] A. Mackin, D. Ma, F. Zhang, D. Bull, A subjective study on videos at various bit depths, in: 2021 Picture Coding Symposium, PCS, IEEE, 2021, pp. 1–5, <http://dx.doi.org/10.1109/PCS50896.2021.9477460>.
- [79] A. Buades, B. Coll, J.-M. Morel, A non-local algorithm for image denoising, in: 2005 IEEE Computer Society Conference on Computer Vision and Pattern Recognition, CVPR'05, Vol. 2, 2005, pp. 60–65 vol. 2, <http://dx.doi.org/10.1109/CVPR.2005.38>.
- [80] L. Chen, X. Chu, X. Zhang, J. Sun, Simple baselines for image restoration, in: S. Avidan, G. Brostow, M. Cissé, G.M. Farinella, T. Hassner (Eds.), Computer Vision – ECCV 2022, Springer Nature Switzerland, 2022, pp. 17–33, http://dx.doi.org/10.1007/978-3-031-20071-7_2.
- [81] O. Ronneberger, P. Fischer, T. Brox, U-net: Convolutional networks for biomedical image segmentation, in: N. Navab, J. Hornegger, W.M. Wells, A.F. Frangi (Eds.), Medical Image Computing and Computer-Assisted Intervention – MICCAI 2015, Springer International Publishing, 2015, pp. 234–241, http://dx.doi.org/10.1007/978-3-319-24574-4_28.
- [82] A. Abdelhamed, S. Lin, M.S. Brown, A high-quality denoising dataset for smartphone cameras, in: 2018 IEEE/CVF Conference on Computer Vision and Pattern Recognition, 2018, pp. 1692–1700, <http://dx.doi.org/10.1109/CVPR.2018.00182>.
- [83] T. Karras, S. Laine, T. Aila, A style-based generator architecture for generative adversarial networks, IEEE Trans. Pattern Anal. Mach. Intell. 43 (12) (2021) 4217–4228, <http://dx.doi.org/10.1109/TPAMI.2020.2970919>.
- [84] Y. Li, W.-G. Cui, H. Huang, Y.-Z. Guo, K. Li, T. Tan, Epileptic seizure detection in EEG signals using sparse multiscale radial basis function networks and the Fisher vector approach, Knowl.-Based Syst. 164 (2019) 96–106, <http://dx.doi.org/10.1016/j.knosys.2018.10.029>.
- [85] S. Katsigiannis, N. Ramzan, DREAMER: A database for emotion recognition through EEG and ECG signals from wireless low-cost off-the-shelf devices, IEEE J. Biomed. Health Inform. 22 (1) (2017) 98–107, <http://dx.doi.org/10.1109/JBHI.2017.2688239>.